Publications of the Astronomical Society of Australia (2024), **41**, e041, 19 pages
doi:10.1017/pasa.2024.38

CAMBRIDGE UNIVERSITY PRESS

Research Article

Mode identification and period fitting in six pulsating hot subdwarfs

S.K. Sahoo[1], A.S. Baran[2,3], P. Németh[4,5], H.L. Worters[6], S. Pramod Kumar[7], S. Joshi[8] and D. Kilkenny[9]

[1]Nicolaus Copernicus Astronomical Centre of the Polish Academy of Sciences, Warsaw, Poland, [2]Department of Physics, Astronomy, and Materials Science, Missouri State University, Springfield, MO, USA, [3]Astronomical Observatory, University of Warsaw, Warszawa, Poland, [4]Astroserver.org, Malomsok, Hungary, [5]Astronomical Institute of the Czech Academy of Sciences, Ondřejov, Czech Republic, [6]South African Astronomical Observatory, Cape Town, South Africa, [7]Indian Institute of Astrophysics, Koramangala, Bangalore, India, [8]Aryabhatta Research Institute of Observational Sciences, Nainital, India and [9]Department of Physics and Astronomy, University of the Western Cape, Bellville, South Africa

Abstract

We report the results of our analysis of six gravity-mode pulsating hot subdwarf stars observed in the short cadence mode by Transiting Exoplanet Survey Satellite. We detected at least 10 pulsation periods in each star, searched for multiplets, and used an asymptotic period spacing to identify modes. We used a grid of evolutionary and pulsation models calculated with the `MESA` and `GYRE`, along with spectroscopic parameters and modal degree identification, to derive the physical properties of the stars. We checked the relation between the helium content and pulsations and found that no pulsator exists among the extremely helium-rich hot subdwarfs, while the number of detected pulsators in other helium groups increases as the helium content decreases. We found p- and g-mode hot subdwarfs pulsators in all Galactic populations.

Keywords: Stars: subdwarfs; stars: oscillations (including pulsations); asteroseismology

(Received 15 March 2024; revised 7 May 2024; accepted 7 May 2024)

1. Introduction

Hot subdwarf stars are located at the extreme blue end of the horizontal branch in the Hertzsprung–Russell diagram (Heber 2016). They divide into different types, depending on spectroscopic parameters (sdB, sdOB, sdO, He-sdB, and He-sdO – see Baran et al. 2023, for details) and observations show that sdB stars are the most common. This work is a continuation of our efforts to detect new hot subdwarf pulsators, understand their internal structure, and connect it to Galactic populations. Hot subdwarfs have a surface gravity $\log(g/\mathrm{cm\,s^{-2}})$ of 5.0–5.8, which indicates that they are compact. In fact, their radii are in a range of 0.15–0.35 $R_\odot$ and their total masses are around 0.5 $M_\odot$ (Heber 2016). According to Figure C4 presented by Ostrowski et al. (2021) the masses can be as low as almost 0.3 $M_\odot$, and they can go beyond 0.5 $M_\odot$ in case of a few solar mass progenitors. The interiors of hot subdwarfs consist of a convective helium core in which helium fusion takes place, surrounded by a helium shell. The outermost layer is a very thin (in mass) hydrogen envelope of less than 10^{-2} $M_\odot$. Such an envelope is a unique mark of hot subdwarfs and is a consequence of some mass loss mechanisms during red-giant branch evolution. The mass loss can be explained by stellar binarity (Han et al. 2002, 2003), substellar companions (Charpinet et al. 2018), or a strong stellar wind (Fontaine et al. 2012). The effective temperature of these stars ranges from 20 000 to 40 000 K. The lack of a massive hydrogen envelope makes hot subdwarfs skip the asymptotic giant branch and evolve directly towards white dwarf cooling tracks. Hot subdwarfs were found in Galactic field populations (Altmann et al. 2004; Martin et al. 2016), old open clusters (Kaluzny and Ruciński 1993), and globular clusters (Moehler 2001; Moni Bidin et al. 2008).

A goal of the kinematic study of stars is to derive their galactic population membership and relationships between populations and specific stellar parameters. Such a study requires large samples of stars for which galactic orbits can be derived. Most of the studies of hot subdwarfs delivered only population membership assignments with no report of a relation between pulsation content and Galactic populations. Colin et al. (1994) determined space velocities and orbits for seven stars and concluded on their Galactic populations. Altmann et al. (2004) performed a kinematic survey of 114 hot subdwarfs. They used space velocities, eccentricities, and angular momenta of their galactic orbits and found that a vast majority of the stars show a kinematic behaviour that is similar to that of thick disc stars. Recently, Luo et al. (2021) performed an extensive kinematics study of 1587 subdwarfs by using precise and uniform Gaia DR2 astrometry and LAMOST DR7 spectroscopy data. The authors derived Galactic population memberships of these stars and tried to find a correlation between the helium content and the membership but came with no conclusions because of a limited sample.

A small subset (around 10%, Østensen et al. 2010; Reed et al. 2021) of hot subdwarfs shows pulsations in pressure (p) modes, gravity (g) modes, or both (hybrids). Stellar pulsations provide us with a pathway to understand their internal structures through asteroseismology (Charpinet et al. 1997). In most cases, p-modes, with typical periods of minutes, provide information about the outer regions, whereas g-modes, with typical periods of hours, probe deeper regions (Heber 2016).

Corresponding author: S.K. Sahoo; Email: sumanta.kumar27@gmail.com

Cite this article: Sahoo SK, Baran AS, Németh P, Worters HL, Pramod Kumar S, Joshi S and Kilkenny D. (2024) Mode identification and period fitting in six pulsating hot subdwarfs. *Publications of the Astronomical Society of Australia* **41**, e041, 1–19. https://doi.org/10.1017/pasa.2024.38

Table 1. Information for the six stars analysed in our work. The 'Reference' column refers to the spectroscopic parameters only.

TIC	Sector	$T_{\rm eff}$ (K)	log (g/cm s^{-2})	log $n_{\rm He}/n_{\rm H}$	G (mag)	Distance (pc)	Reference
262753627	33,44-46	24 670 (320)	5.51 (3)	−2.76 (14)	12.44	401 (9)	This work
		25 790 (160)	5.43 (1)	−2.65 (4)			Lei et al. (2018)
269766236	27	26 880 (1500)	5.41 (12)	−3.06 (47)	13.39	648 (15)	This work
298109741	15-16,21-22,48-49	25 780 (460)	5.51 (7)	−2.68 (11)	13.12	719 (15)	This work
		25 010	5.04	–			Billères et al. (2002)
311432346	25-26,52-53	25 380 (990)	5.54 (18)	−2.63 (+ 0.48; − 1.26)	10.29	293 (3)	Vos et al. (2013)
331553315	19,25-26,52-53,59	26 800 (700)	5.4 (1)	−3.0 (2)	13.71	715 (12)	Edelmann et al. (2003)
367003034	17-19,24-25,52,57,59	28 070 (370)	5.82 (10)	−3.48 (42)	13.61	653 (8)	This work

The Transiting Exoplanet Survey Satellite (TESS; Ricker et al. 2014) is an all-sky survey whose prime mission is to detect exoplanets orbiting nearby bright stars using the transit method. Apart from its prime mission, it also provides time-series photometry of a large sample of stars, which can be used for other goals, including asteroseismology. We only included a selection of results of analyses of hot subdwarf pulsators derived with TESS. Charpinet et al. (2019) presented a detailed asteroseismic analysis of EC 21494–7018 (TIC 278659026), a pulsating sdB star with 20 gravity modes, which was monitored in the short cadence (SC) mode (2 min). Reed et al. (2020) reported analysis of CD – 28° 1974. They found the gravity-mode frequency range to be slightly different than the typical for these stars and concluded that the star must have a different internal structure. Sahoo et al. (2020a) presented a detailed mode identification and atmospheric analyses of three pulsating hot subdwarfs. Uzundag et al. (2021) presented photometric and spectroscopic analyses of five gravity-mode hot subdwarf pulsators observed in the SC, as well as ultra-short cadence (20 sec) modes. Silvotti et al. (2022) reported an analysis of a hot subdwarf pulsator, TYC 4544-2658-1, found to be a non-synchronised binary system with the shortest orbital and core rotation periods. The authors reported rotationally split modes, provided a mode identification, and matched observed pulsation periods with modelled ones. Sahoo et al. (2020b) and Baran et al. (2021) used TESS Full Frame Images to find new variable hot subdwarfs and performed mode identification for a few pulsators. Baran et al. (2023) presented a list of p-mode hot subdwarf pulsators observed by TESS. We report the results of our analysis of the TESS photometry of six hot subdwarf pulsators, that is, TIC 262753627, TIC 269766236, TIC 298109741, TIC 311432346, TIC 331553315, and TIC 367003034. We selected six stars with a moderate number of g-modes, which can be identified using asymptotic period spacing, followed by pulsation periods fitting. Prior to this work, only for five pulsating hot subdwarfs `MESA` and `GYRE` models (acronyms are explained in Section 4) were used to derive stellar parameters (Silvotti et al. 2022; Baran & Sanjayan 2023).

2. TESS photometry and ground-based spectroscopy

TESS provided data for all six targets in the SC mode and for TIC 298109741, TIC 311432346, TIC 331553315, and TIC 367003034 in the USC mode, which became available only with the onset of the extended mission. We downloaded the data from the Mikulski Archive for Space Telescopes (MAST) database. Only TIC 269766236 was observed during a single sector covering about 27 days. The remaining five stars were monitored over multiple sectors, ranging from four to eight for the longest data coverage. We combined datasets if they were collected during a single observing cycle and provided roughly the same solutions as compared to those derived from shorter chunks; with the exception of frequencies that are low amplitude and did not meet the threshold criterion, as a consequence of a higher noise level in amplitude spectra in shorter chunks of data. More details of each star are given in Table 1. We used PDCSAP_FLUX measures, which account for onboard systematics and a contribution from neighbouring stars. We detrended variations longer than one day and converted the fluxes to a parts per thousand (ppt) unit. We used `Lightkurve` (Lightkurve Collaboration et al. 2018) to process the data.

Table 2. Details of spectroscopic observations of four stars observed using ground-based telescopes.

TIC	Date	Site	$t_{\rm exp}$ (s)	Resolution	SNR
262753627	27 Feb 2013	LAMOST	1 800	2 000	82
269766236	05 Jun 2021	SAAO	200	1 000	208
298109741	12 Apr 2021	APO	1 800	2 400	143
367003034	12 Jul 2022	IAO	300	1 200	27

We collected atmospheric parameters of TIC 262753627, TIC 298109741, TIC 311432346, and TIC 331553315 from the literature and listed them in Table 1. In addition, we acquired an existing LAMOST spectrum of TIC 262753627, and we collected spectroscopic observations of TIC 269766236 with the 1.9 m telescope at the South African Astronomical Observatory (SAAO), of TIC 298109741 with the Dual Imaging Spectrograph at Apache Point Observatory, and of TIC 367003034 with the Hanle Faint Object Spectrograph Camera (HFOSC) of 2 m Himalayan Chandra Telescope (HCT) at the Indian Astronomical Observatory (IAO). Details of our spectroscopic observations are listed in Table 2.

We analysed the spectra with the data-driven steepest-descent χ^2 minimisation spectral analysis program XTGRID (Németh et al. 2012) to determine effective temperature ($T_{\rm eff}$), surface gravity (log g), and helium abundance ($n_{\rm He}/n_{\rm H}$). The fitting procedure

https://doi.org/10.1017/pasa.2024.38 Published online by Cambridge University Press

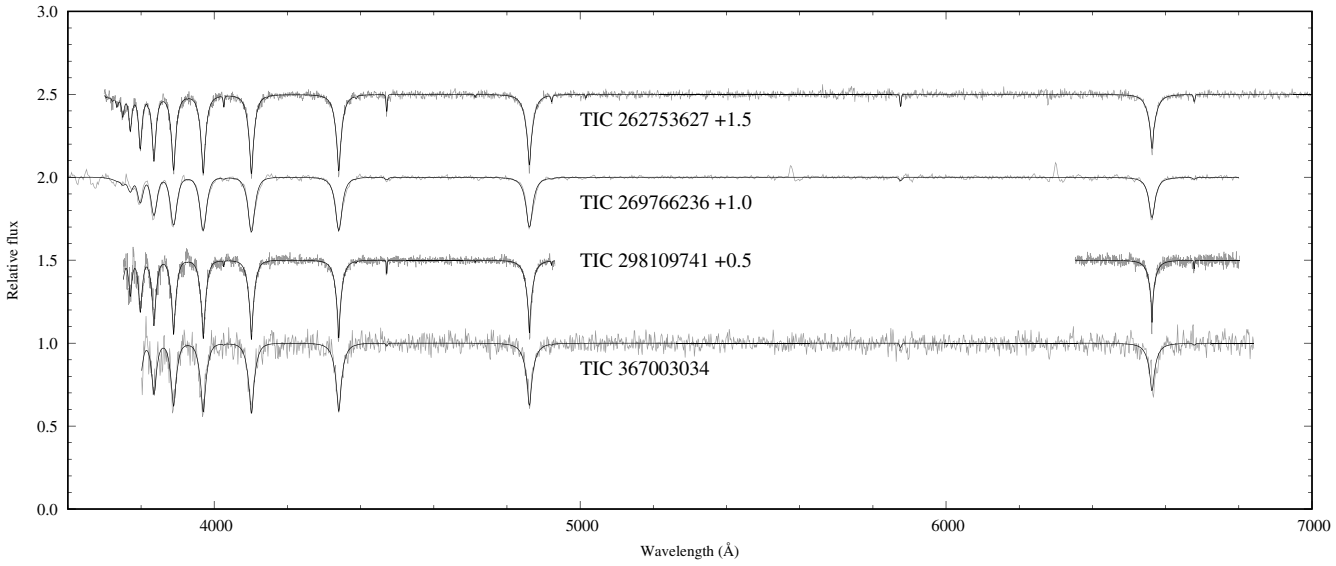

Figure 1. Best-fit TLUSTY/XTGRID models to the various observations of the program stars: TIC 262753627 (LAMOST), TIC 269766236 (SAAO), TIC 298109741 (APO), and TIC 367003034 (HFOSC). In all cases, observations are in grey and the models are in black.

is an interface to calculate non-LTE (non-Local Thermodynamic Equilibrium) stellar atmosphere models and synthetic spectra with TLUSTY/SYNSPEC (Hubeny and Lanz 1995, 2017) and to fit them to observations. The theoretical models are matched to the observations with piecewise normalisation, and the model parameters are varied iteratively along the steepest gradient of the global χ^2 until the fit converges to the best solution. The normalisation method reduces the effects of the uncalibrated continuum flux and the fit is based on the relative strengths and profiles of the spectral lines. The fitting procedure iterates the models until the relative changes of all model parameters and the χ^2 decrease below 0.1% over three consecutive iterations. Then, parameter errors are calculated by mapping the χ^2 variations around the best solution. For $T_{\rm eff}$ and $\log g$, this includes the correlations in two dimensions, and for the He abundance it is done in one dimension. If a better solution is found during error calculations XTGRID returns to iterations with the local minimum as starting point. More details on the procedure can be found in Németh et al. (2012).

Our models included H and He opacities in both the stellar structure calculations and the spectral synthesis. The final parameters are listed in Table 1, and the best-fit models are shown in Fig. 1. Parameter degeneracies are large in low-resolution spectroscopy, which are reflected by the large measured statistical errors. A significantly larger systematic error than degeneracies is introduced by calibration issues, and flexure, which affected the SAAO spectrum. The large parameter uncertainties for TIC 269766236 are due to the non-symmetric and non-Gaussian instrumental profile of grating #7 of the SpUpNIC spectrograph on the 1.9 m telescope at SAAO (Figure 21 in Crause et al. 2019).

3. Fourier analysis and mode identification

We calculated amplitude spectra, and we applied a standard prewhitening process with `Period04` (Lenz and Breger 2005). We fitted significant signal with $A_i \sin(2\pi {\rm f_i} {\rm t} + \phi_{\rm i})$ using a nonlinear least-square method. The symbols used have usual meaning, that is, A is amplitude, f is frequency, ϕ is phase, while 'i' iterates through the sinusoidal terms. We limited the detection threshold to be five times the median noise (N) level (Baran andKoen 2021), which was calculated from residual amplitude spectra in the range of 1 000–4 000 μHz. The corresponding Nyquist frequency is 4 166 μHz. We detected no signal beyond 4 166 μHz in the USC data, hence we limit our analyses only to the SC mode for all six targets. A few frequencies with amplitudes lower than the threshold, listed in Tables 3, 4, and 7, should be considered tentative. We discuss details of our prewhitening and mode identification for each target in the paragraphs below.

We determined the mode degree using the asymptotic period spacing, widely applied and described in previous works (Østensen et al. 2014). In the asymptotic limit ($n \gg l$), consecutive g-mode overtones, for a given degree, are evenly spaced in period. An average period spacing of dipole modes (l=1) ranges from 230 to 270 s (e.g. Reed et al. 2020; Sahoo et al. 2020*a*). We started our modal degree assignment from the highest amplitude frequencies and assigned them dipole modes if a period spacing was a multiple of about 250 s. Next, other frequencies with lower amplitudes, but spaced as the highest amplitude counterparts, were also assigned with dipole modes. Our choice can be justified by the surface cancellation effect (Dziembowski 1977), which dilutes an amplitude as the mode degree increases by approximately $(1/\sqrt{l})$. In our analyses, the majority of the detected frequencies are dipole modes, hence we only calculated the average period spacings for dipole modes. We used a linear regression to derive average period spacings and uncertainties of dipole modes. We calculated the average period spacings and their uncertainties for quadrupole modes from equation $\Delta P_{l=2} = \Delta P_{l=1}/\sqrt{3}$. Since we found no multiplets in any of our targets, the mode assignment based solely on the period spacing sequences may not always be correct.

Most frequencies were identified as dipole modes with just a handful of exceptions for each target. After determining the dipole modes, we tried to match the rest of the spacing with the quadrupole sequence. But we stress that due to very limited numbers of detected quadrupole modes, the trends in the échelle diagrams are more scattered and these solutions may not be unique.

https://doi.org/10.1017/pasa.2024.38 Published online by Cambridge University Press

Table 3. Frequencies detected in amplitude spectra of TIC 262753627. An apostrophe sign denotes signals taken for analysis presented in Section 4.

ID	Frequency (μHz)	Period (s)	Amplitude (ppt)	S/N	*l*	*n*
		Sector 33				
f_1	131.539(13)	7 602.3(7)	1.35(7)	16.8	1'	33
f_2	133.709(14)	7 478.9(8)	1.25(7)	15.4	–	–
f_3	140.116(21)	7 137.0(1.1)	0.82(7)	10.1	1'	31
f_4	161.209(27)	6 203.1(1.1)	0.62(7)	7.7	1'	27
f_5	167.287(13)	5 977.73(47)	1.29(7)	16.0	1'	26
f_6	197.829(12)	5 054.87(30)	1.45(7)	18.0	1'	22
f_7	217.612(14)	4 595.33(31)	1.17(7)	14.6	1'	20
f_8	229.78(34)	4 351.98(65)	0.50(7)	6.2	1'	19
f_9	235.288(22)	4 250.11(39)	0.79(7)	9.7	2	32
f_{10}	243.566(23)	4 105.66(38)	0.75(7)	9.3	1'	18
f_{11}	258.317(11)	3 871.21(17)	1.54(7)	19.1	1'	17
f_{12}	274.193(30)	3 647.06(40)	0.57(7)	7.0	1'	16
f_{13}	313.813(43)	3 186.61(43)	0.40(7)	4.9	1	14
f_{14}	344.381(16)	2 903.76(13)	1.09(7)	13.5	2	22
		Sectors 44–46				
f_1	109.933(13)	9 096.5(1.0)	0.292(45)	5.8	1	39
f_2	119.619(13)	8 359.9(9)	0.293(45)	5.8	1	36
f_3	125.601(11)	7 961.7(7)	0.330(45)	6.5	2	60
f_4	127.068(6)	7 869.80(36)	0.626(45)	12.3	1'	34
f_5	133.7107(48)	7 478.84(27)	0.773(45)	15.3	–	–
f_6	140.103(12)	7 137.6(6)	0.307(45)	6.1	1'	31
f_7	161.307(10)	6 199.36(39)	0.363(45)	7.2	1'	27
f_8	167.1801(37)	5 981.57(13)	0.997(45)	19.7	1'	26
f_9	186.639(10)	5 357.93(28)	0.373(45)	7.4	2	40
f_{10}	197.7612(33)	5 056.60(8)	1.113(45)	22.0	1'	22
f_{11}	207.131(9)	4 827.86(21)	0.403(45)	8.0	1	21
f_{12}	217.6118(32)	4 595.34(7)	1.145(45)	22.6	1'	20
f_{13}	221.0221(53)	4 524.43(11)	0.691(45)	13.6	2	34
f_{14}	229.790(13)	4 351.79(24)	0.293(45)	5.8	1'	19
f_{15}	232.397(9)	4 302.98(17)	0.399(45)	7.9	–	–
f_{16}	243.5757(59)	4 105.50(10)	0.629(45)	12.4	1'	18
f_{17}	258.3152(26)	3 871.239(39)	1.406(45)	27.7	1'	17
f_{18}	274.160(8)	3 647.51(10)	0.483(45)	9.5	1'	16
f_{19}	289.430(12)	3 455.07(14)	0.305(45)	6.0	2	26
f_{20}	344.3618(44)	2 903.922(37)	0.842(45)	16.6	2	22

Periods not matching either dipole or quadrupole sequences were marked as unidentified. As described in Sahoo et al. (2020a) the radial order n is not absolute. Based on our mode assignment, we calculated échelle diagrams for dipole and quadrupole modes. The former ones tend to show vertical trends, often distorted by a side hook centred around 5 000 s. These hooks were previously reported by Baran andWinans (2012). The quadrupole modes are very sparse and for most targets, they do not show vertical trends, which could support our l=2 assignment. We cannot exclude that some of the low-amplitude or unidentified modes could be either $l > 2$, or trapped modes.

Table 4. Frequencies detected in an amplitude spectrum of TIC 269766236.

ID	Frequency (μHz)	Period (s)	Amplitude (ppt)	S/N	*l*	*n*
		Sector 27				
f_1	116.704(50)	8 568.7(3.7)	0.65(12)	4.5	1	36
f_2	183.151(18)	5 459.98(53)	1.79(12)	12.5	1'	22
f_3	190.724(45)	5 243.2(1.2)	0.72(12)	5.0	2	35
f_4	211.238(14)	4 734.00(32)	2.22(12)	15.5	1'	19
f_5	222.955(42)	4 485.2(9)	0.76(12)	5.3	1	18
f_6	235.835(24)	4 240.25(42)	1.36(12)	9.5	1'	17
f_7	265.494(29)	3 766.56(41)	1.11(12)	7.7	1'	15
f_8	306.078(17)	3 267.14(19)	1.84(12)	12.8	1'	13
f_9	331.019(24)	3 020.97(22)	1.35(12)	9.4	1'	12
f_{10}	354.312(26)	2 822.37(21)	1.24(12)	8.6	2	19
f_{11}	367.903(26)	2 718.11(19)	1.24(12)	8.6	–	–

TIC 262753627. (TYC 770-941-1) was recognised as an sdB star from the LAMOST survey by Lei et al. (2018). The spectroscopic parameters reported by the authors and those we derived from a fit to our spectrum are listed in Table 1. Pulsations in this star were detected by Sahoo et al. (2020b). After the initial discovery of a significant signal in the long cadence (30 min) data, it was reobserved in the SC mode in Sectors 33 and 44–46. In the Sector 33 data, we detected 14 frequencies, out of which 11 were identified as dipole and two as quadrupole modes. We estimated an average period spacing of 232.59 (41) s and 134.29(24) s for dipole and quadrupole modes, respectively. In the combined Sectors 44–46 data, we detected 20 frequencies, out of which 13 were dipole and 5 were quadrupole modes. The average period spacings equals 235.7(8) s and 136.09(44) s for dipole and quadrupole modes, respectively. A difference between the average period spacings estimated in both two datasets are larger than their uncertainties. It is a consequence of some of the periods changed between datasets, which in turn, can be real and caused by the physical change of a pulsation cavity. In such cases, we consider period spacings and échelle diagrams separately. We list the frequencies in Table 3, plot amplitude spectrum in Fig. 2, and échelle diagrams in Fig. 3.

TIC 269766236. (Gaia DR2 6697530086799358720) was found to be a hot subdwarf candidate by Geier et al. (2019). A fit to our spectrum revealed that this star is hotter and more compact than a typical g-mode dominated sdB pulsator. The star was observed by TESS during Sector 27. We detected 11 pulsation frequencies, which are listed in Table 4. No rotationally split modes were found. Using an asymptotic period spacing we marked seven dipole and three quadrupole modes. Frequency f_{11} does not fit either dipole or quadrupole sequences, and we left it unidentified. We derived an average period spacing for dipole modes to be 241.0(6) s, and for quadrupole modes to be 139.15(35) s. We list the frequencies in Table 4, plot the amplitude spectrum in Fig. 4, and échelle diagrams in Fig. 5.

TIC 298109741. (PG 1340+607) was identified as an sdB star by Green et al. (1986). We confirm this spectral type with the spectroscopic parameters listed in Table 1. The star was observed by TESS during Sectors 15–16, 21–22, and 48–49. After examining

https://doi.org/10.1017/pasa.2024.38 Published online by Cambridge University Press

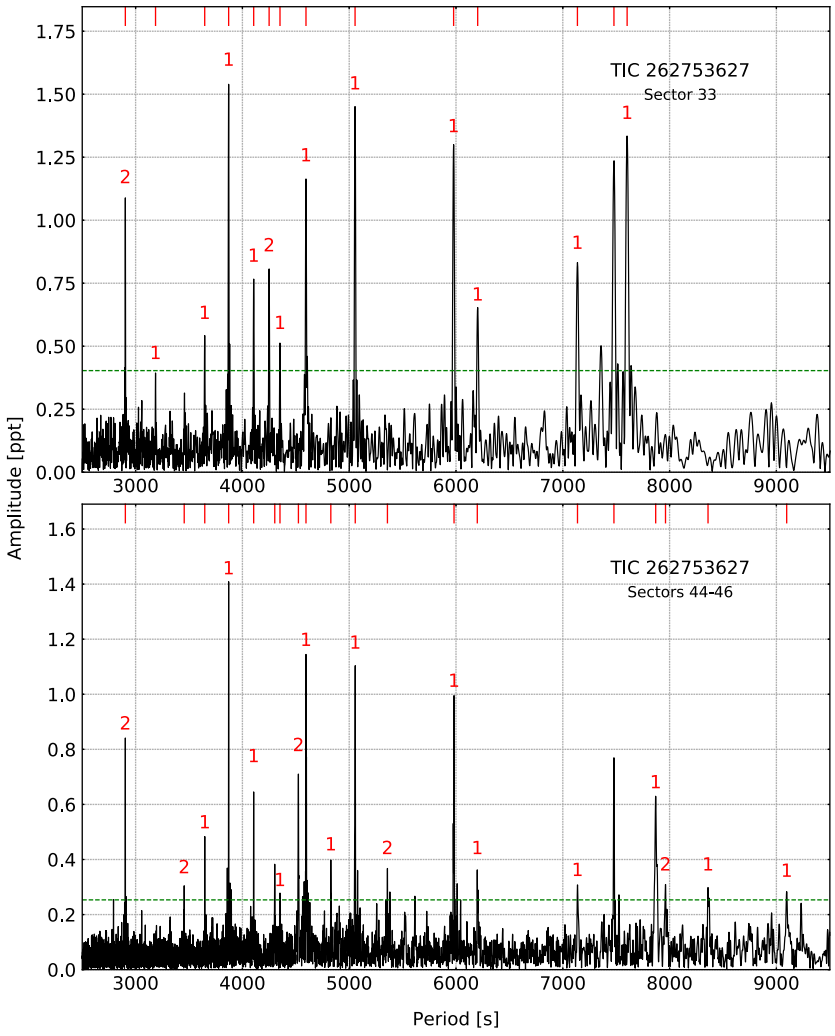

Figure 2. Amplitude spectra calculated from the SC data collected in different TESS sectors for TIC 262753627. The horizontal green dashed line denotes the detection threshold. Modal degrees are shown on top of each identified mode.

each set individually, we combined Sector 15–16 and 21–22 data and prewhitened 19 frequencies in the range of 70–280 μHz. No multiplets were found. We applied an asymptotic period spacing and identified 14 frequencies as dipole and 5 as quadrupole modes. We estimated an average period spacing for dipole modes to be 250.96(52) s, and for the quadrupole modes to be 144.89(30) s. We also combined the data from Sector 48–49 and detected 14 frequencies (12 dipole and 2 quadrupole modes). The average period spacings were within the uncertainties of the Sector 15–16 and 21–22 data. The average period spacings were 251.38(48) s for dipole and 145.13(28) s for quadrupole modes. A difference between the average period spacings is not significant, hence we calculated the average of those two values and used this value to calculate échelle diagrams for both datasets. The average period spacings calculated from all data equals 251.17(35) s and 145.01(21) s for dipole and quadrupole modes, respectively. We list the frequencies in Table 5, plot the amplitude spectra in Fig. 6, and échelle diagrams in Fig. 7.

TIC 311432346. (BD+29 3070) was listed as an sdOB+F star in the catalogue of hot subdwarfs (Kilkenny et al. 1988). Spectroscopic parameters derived by Vos et al. (2013) indicate the star to be an sdB with a main sequence companion. The star was observed by TESS during Sector 25–26 and 52–53. Our analysis of the Sector 25–26 data revealed 22 significant frequencies. The lowest frequency (near 7.74 μHz) appears to have a strong first harmonic, and it can be interpreted either as binarity or the rotation of stellar spots on the main sequence companion. Since the amplitude of a flux variation is not stable over time we lean towards the latter explanation. The period of 1.49516(34) d, is quite different from the 1 283(63) days reported by Vos et al. (2013). We detected 20 g-mode pulsations, but we found no multiplets. Using an asymptotic period spacing we identified 14 dipole and three quadrupole modes. We left two frequencies unidentified. The average period spacings are 254.87(38) s for dipole and 147.15(22) s for quadrupole modes, respectively. Our analysis of the Sectors 52–53 data revealed 14 frequencies, including two low frequencies discussed in the previous paragraph. Out of 12 pulsation frequencies, we identified nine as dipole modes, two as quadrupole modes. The average period spacings we calculated are 253.9(8) s and 146.61(43) s for dipole and quadrupole modes, respectively. The average period spacings calculated from all data

https://doi.org/10.1017/pasa.2024.38 Published online by Cambridge University Press

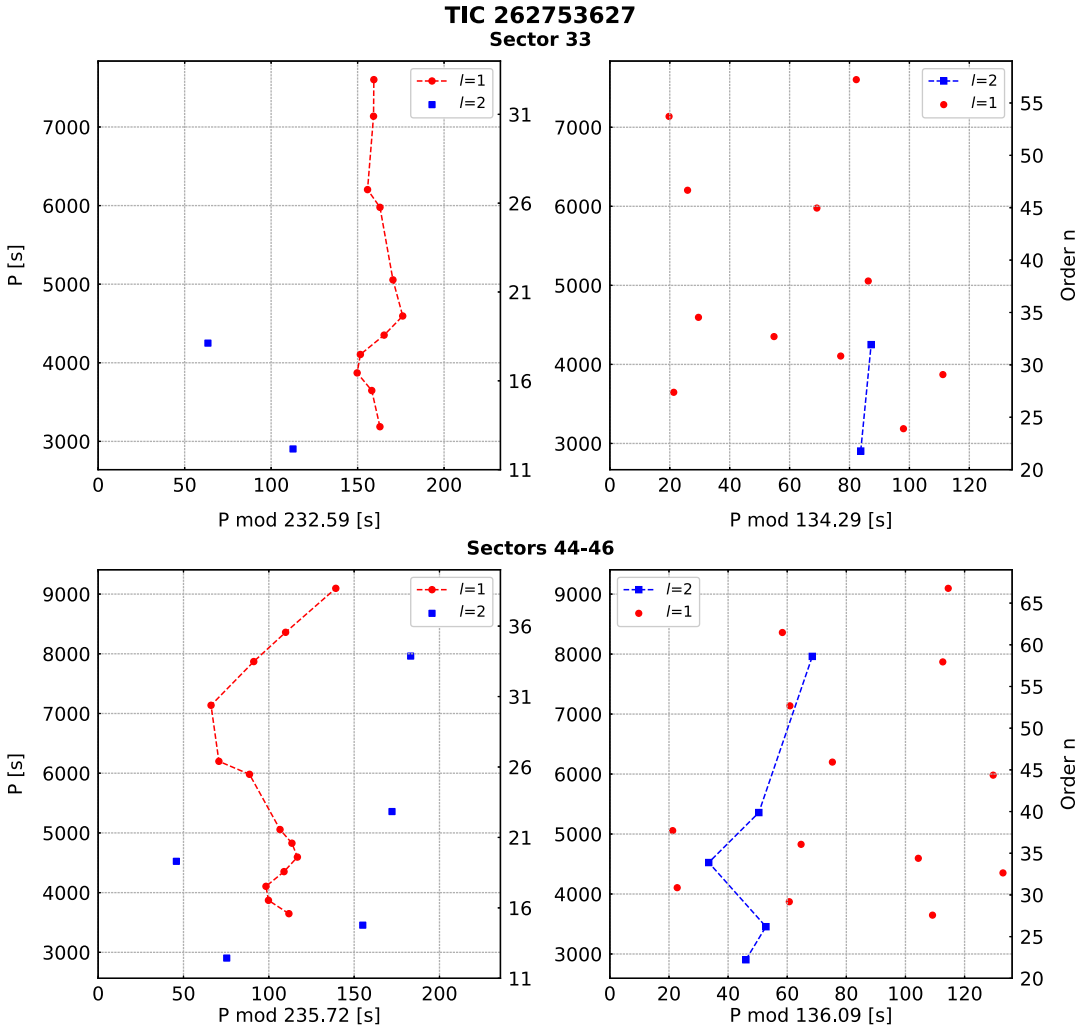

Figure 3. Échelle diagrams derived for SC data collected in different TESS sectors for TIC 262753627.

equals 254.39(44) s for dipole and 146.88(24) s for quadrupole modes. We list the frequencies in Table 6, plot the amplitude spectra in Fig. 8, and échelle diagrams in Fig. 9.

TIC 331553315. (HS 0430+7712) was classified as an sdB star by Edelmann et al. (2003), and we list the spectroscopic parameters in Table 1. It was among 285 hot subdwarfs observed by Østensen et al. (2010) using the Nordic Optical Telescope (NOT) but no variability was found. TESS observed the star during Sector 19, 25–26 52–53, and 59. After examining each set individually, we combined Sector 19 with Sectors 25–26 and detected 14 g-mode frequencies. By means of the asymptotic period spacing, we identified 11 dipole and three quadrupole modes. The average period spacings are 258.8(1.1) s and 149.4 (6) s for dipole and quadrupole modes, respectively. We found no rotationally split modes. From the combined Sector 52–53 and 59 data, we detected 12 frequencies, out of which we marked nine as dipole and three as quadrupole modes. The average period spacings are 257.7(2.0) s and 148.8(1.2) s for dipole and quadrupole modes, respectively. The average period spacings calculated from all data equals 258.3(1.1) s for dipole and 149.1(7) s for quadrupole modes.

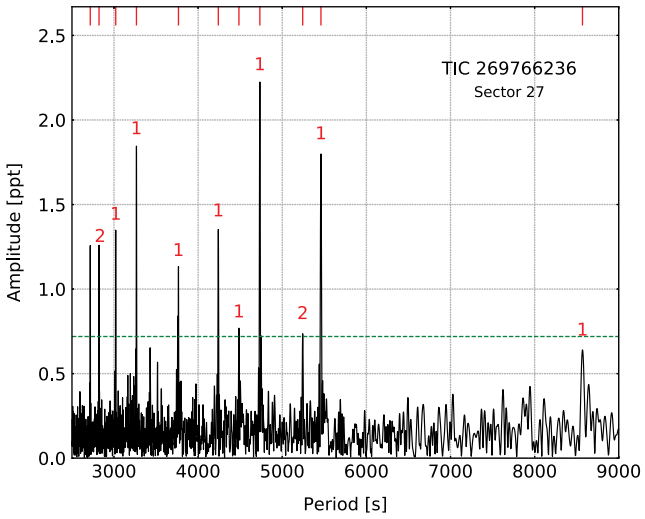

Figure 4. An amplitude spectrum for TIC 269766236. The horizontal green dashed line denotes the detection threshold. Modal degrees are shown on top of each identified mode.

https://doi.org/10.1017/pasa.2024.38 Published online by Cambridge University Press

Table 5. Frequencies detected in amplitude spectra of TIC 298109741.

ID	Frequency (μHz)	Period (s)	Amplitude (ppt)	S/N	*l*	*n*
		Sectors 15–16,21–22				
f_1	72.9659(16)	13 705.04(30)	0.885(47)	16.2	1	55
f_2	83.8450(45)	11 926.77(63)	0.313(47)	5.7	1	48
f_3	89.8315(34)	11 131.95(43)	0.406(47)	7.4	1	45
f_4	109.0063(14)	9 173.78(12)	0.982(47)	18.0	1’	37
f_5	131.2634(44)	7 618.27(26)	0.313(47)	5.7	2	53
f_6	135.1020(34)	7 401.81(18)	0.414(47)	7.6	1’	30
f_7	144.6050(14)	6 915.39(7)	0.997(47)	18.3	1’	28
f_8	161.7488(7)	6 182.427(26)	2.055(47)	37.6	1’	25
f_9	168.4455(9)	5 936.639(33)	1.483(47)	27.1	1’	24
f_{10}	175.9229(34)	5 684.31(11)	0.407(47)	7.5	1	23
f_{11}	184.3296(35)	5 425.06(10)	0.399(47)	7.3	1’	22
f_{12}	199.3807(31)	5 015.53(8)	0.454(47)	8.3	2	35
f_{13}	211.7586(22)	4 722.36(49)	0.635(47)	11.6	2	33
f_{14}	227.0665(10)	4 404.00(20)	1.384(47)	25.3	1’	18
f_{15}	233.5807(43)	4 281.18(8)	0.321(47)	5.9	2	30
f_{16}	241.5041(16)	4 140.717(27)	0.895(47)	16.4	1’	17
f_{17}	258.5155(26)	3 868.239(25)	0.852(47)	15.6	1’	16
f_{18}	275.9906(21)	3 623.312(27)	0.674(47)	12.3	1	15
f_{19}	279.7006(18)	3 575.251(23)	0.763(47)	14.0	2	25
		Sectors 48–49				
f_1	72.983(9)	13 701.8(1.7)	0.82(7)	10.6	1	55
f_2	109.004(18)	9 173.9(1.5)	0.41(7)	5.3	1’	37
f_3	118.849(17)	8 414.1(1.2)	0.42(7)	5.5	1	34
f_4	126.440(15)	7 908.9(9)	0.49(7)	6.3	1	32
f_5	135.074(18)	7 403.3(1.0)	0.41(7)	5.3	1’	30
f_6	144.603(9)	6 915.48(44)	0.80(7)	10.3	1’	28
f_7	161.7548(33)	6 182.20(13)	2.24(7)	28.8	1’	25
f_8	168.452(6)	5 936.41(22)	1.16(7)	14.9	1’	24
f_9	184.335(11)	5 424.88(33)	0.65(7)	8.4	1’	22
f_{10}	211.685(9)	4 723.99(20)	0.81(7)	10.4	2	33
f_{11}	227.0890(56)	4 403.56(11)	1.31(7)	16.9	1’	18
f_{12}	241.527(6)	4 140.32(11)	1.18(7)	15.1	1’	17
f_{13}	258.556(13)	3 867.63(19)	0.58(7)	7.5	1’	16
f_{14}	279.693(9)	3 575.35(11)	0.84(7)	10.8	2	25

We list the frequencies in Table 7, plot amplitude spectra in Fig. 10 and échelle diagrams in Fig. 11.

TIC 367003034. (GALEX J223336.8+741254) was identified as an sdB star by Geier et al. (2017); a fit to our spectrum confirms that identification. As with TIC 269766236, the fit results in a rather high surface gravity for a g-mode hot subdwarf. Boudreaux et al. (2017) searched for pulsations in the GALEX data reporting a frequency of 7 891 μHz. TESS observed the star during Sector 17–19, 24–25, 52, 57, and 59. We merged the Sector 17–19, 24–25 data and detected 12 g-mode frequencies. We found nine dipoles, one quadrupole, and one could not be defined. We estimated an average period spacing for dipole modes to be 266.8(1.8) s and for quadrupole modes to be 154.0(1.1). From the combined Sector 52, 57 and 59 data, we detected eight frequencies out of which we marked six as dipole and two as quadrupole modes. The average period spacings are 271.1(1.4) and 156.5(8) for dipole and quadrupole modes, respectively. We list the frequencies in Table 8, plot the amplitude spectra in Fig. 12 and échelle diagrams in Fig. 13.

Table 6. Frequencies detected in amplitude spectra of TIC 311432346. An apostrophe sign denotes signals taken for analysis presented in Section 4.

ID	Frequency (μHz)	Period (s)	Amplitude (ppt)	S/N	*l*	*n*
		Sectors 25–26				
Ω	7.7410(17)	129 182(29)	0.558(12)	78.1	–	–
2Ω	15.1442(27)	66 032(12)	0.525(12)	49.9	–	–
f_1	88.312(16)	11 323.4(2.1)	0.097(12)	8.4	–	–
f_2	91.960(9)	10 874.2(1.1)	0.168(12)	14.5	1	43
f_3	107.164(20)	9 331.5(1.7)	0.080(12)	6.9	1	37
f_4	113.388(10)	8 819.3(7)	0.164(12)	14.2	1	35
f_5	124.265(20)	8 047.3(1.3)	0.079(12)	6.9	1	32
f_6	132.842(16)	7 527.7(9)	0.099(12)	8.6	1’	30
f_7	137.4661(28)	7 274.52(15)	0.553(12)	47.8	1’	29
f_8	147.694(16)	6 770.8(7)	0.097(12)	8.4	1	27
f_9	153.292(7)	6 523.49(31)	0.219(12)	18.9	1’	26
f_{10}	173.1751(19)	5 774.503(65)	0.806(12)	69.7	1’	23
f_{11}	180.9368(26)	5 526.79(8)	0.612(12)	52.9	1’	22
f_{12}	199.7732(57)	5 005.68(14)	0.274(12)	23.6	1’	20
f_{13}	202.314(16)	4 942.81(39)	0.097(12)	8.4	2	34
f_{14}	206.7651(59)	4 836.41(14)	0.274(12)	22.9	–	–
f_{15}	237.3201(17)	4 213.72(30)	0.092(12)	8.0	–	–
f_{16}	238.0154(12)	4 201.41(21)	0.130(12)	11.2	2	29
f_{17}	247.0737(51)	4 047.38(8)	0.305(12)	26.4	2	28
f_{18}	251.137(8)	3 981.89(12)	0.200(12)	17.3	1’	16
f_{19}	269.104(8)	3 716.03(10)	0.208(12)	18.0	1’	15
f_{20}	288.6923(48)	3 463.896(57)	0.330(12)	28.5	1’	14
		Sectors 52–53				
Ω	7.7445(21)	129 123(35)	0.858(13)	66.8	–	–
2Ω	15.2071(45)	65 759(19)	0.401(13)	31.2	–	–
f_1	132.912(6)	7 523.79(33)	0.313(13)	24.4	1’	30
f_2	137.442(6)	7 275.82(33)	0.292(13)	22.7	1’	29
f_3	153.3816(45)	6 519.69(20)	0.390(13)	30.4	1’	26
f_4	173.2859(58)	5 770.81(19)	0.312(13)	24.3	1’	23
f_5	180.9548(26)	5 526.24(8)	0.712(13)	55.4	1’	22
f_6	199.7807(50)	5 005.49(13)	0.365(13)	28.4	1’	20
f_7	206.764(8)	4 836.44(18)	0.241(13)	18.8	–	–
f_8	247.0815(6)	4 047.25(10)	0.296(13)	23.0	2	28
f_9	251.1450(56)	3 981.76(9)	0.326(13)	25.4	1’	16
f_{10}	269.125(6)	3 715.75(9)	0.294(13)	22.9	1’	15
f_{11}	288.7090(54)	3 463.70(6)	0.339(13)	26.4	1’	14
f_{12}	315.953(14)	3 165.03(14)	0.128(13)	10.0	2	22

https://doi.org/10.1017/pasa.2024.38 Published online by Cambridge University Press

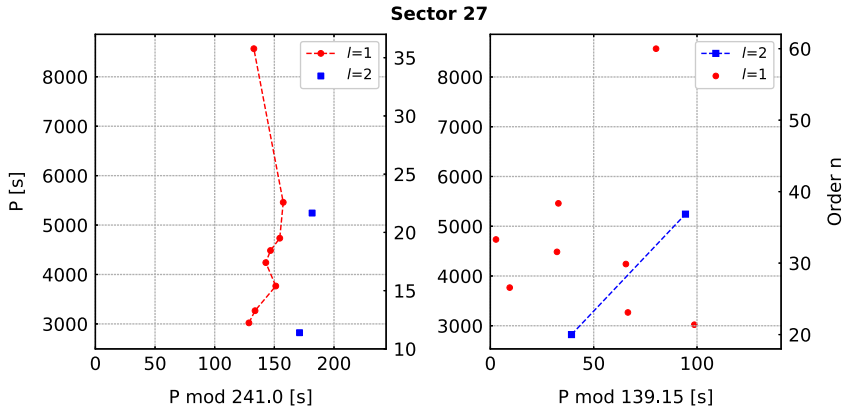

Figure 5. Échelle diagrams for TIC 269766236.

Table 7. Frequencies detected in amplitude spectra of TIC 331553315. An apostrophe sign denotes signals taken for analysis presented in Section 4.

ID	Frequency (μHz)	Period (s)	Amplitude (ppt)	S/N	*l*	*n*
		Sectors 19,25–26				
f_1	108.5481(36)	9 212.51(30)	0.88(11)	6.9	1	36
f_2	130.4171(47)	7 667.71(27)	0.67(11)	5.3	1	30
f_3	170.6954(23)	5 858.39(8)	1.36(11)	10.7	1’	23
f_4	178.7228(37)	5 595.26(12)	0.85(11)	6.7	1’	22
f_5	195.6089(47)	5 112.24(12)	0.67(11)	5.3	1	20
f_6	206.3437(26)	4 846.283(61)	1.20(11)	9.5	1’	19
f_7	229.9227(39)	4 349.29(7)	0.81(11)	6.3	1’	17
f_8	246.8725(32)	4 050.674(53)	0.98(11)	7.7	1’	16
f_9	251.3087(42)	3 979.170(66)	0.75(11)	5.9	2	28
f_{10}	261.0003(25)	3 831.413(37)	1.26(11)	9.9	2	27
f_{11}	263.9061(17)	3 789.227(24)	1.86(11)	14.6	1’	15
f_{12}	271.9440(24)	3 677.228(33)	1.29(11)	10.1	2	26
f_{13}	284.4170(23)	3 515.964(28)	1.39(11)	11.0	1’	14
f_{14}	336.5459(27)	2 971.363(24)	1.17(11)	9.2	1’	12
		Sectors 52–53,59				
f_1	140.7597(51)	7 104.31(26)	0.56(10)	4.9	1	28
f_2	170.7678(23)	5 855.90(8)	1.25(10)	11.1	1’	23
f_3	178.7339(23)	5 594.91(7)	1.25(10)	11.2	1’	22
f_4	206.4534(38)	4 843.71(9)	0.74(10)	6.5	1’	19
f_5	229.9233(27)	4 349.276(52)	1.03(10)	9.2	1’	17
f_6	246.9390(33)	4 049.584(53)	0.87(10)	7.7	1’	16
f_7	251.2984(51)	3 979.33(8)	0.56(10)	5.0	2	28
f_8	260.9897(37)	3 831.569(55)	0.75(10)	6.7	2	27
f_9	263.8974(17)	3 789.351(24)	1.68(10)	14.9	1’	15
f_{10}	271.8161(29)	3 678.958(40)	0.96(10)	8.5	2	26
f_{11}	284.4258(26)	3 515.856(31)	1.11(10)	9.9	1’	14
f_{12}	336.4516(33)	2 972.196(29)	0.86(10)	7.7	1’	12

Table 8. Frequencies detected in amplitude spectra of TIC 367003034. An apostrophe sign denotes signals taken for analysis presented in Section 4.

ID	Frequency (μHz)	Period (s)	Amplitude (ppt)	S/N	*l*	*n*
		Sectors 17–19,24–25				
f_1	154.5309(24)	6 471.20(10)	0.87(8)	9.2	1	25
f_2	183.4856(25)	5 450.02(8)	0.83(8)	8.8	1’	21
f_3	202.7675(16)	4 931.756(39)	1.34(8)	14.1	1’	19
f_4	214.5555(13)	4 660.798(29)	1.60(8)	16.9	1’	18
f_5	227.8255(25)	4 389.324(48)	0.85(8)	9.0	1’	17
f_6	278.1650(38)	3 594.989(49)	0.55(8)	5.9	1	14
f_7	298.0138(44)	3 355.549(49)	0.49(8)	5.1	2	21
f_8	303.4131(27)	3 295.836(30)	0.77(8)	8.2	1	13
f_9	303.6883(39)	3 292.850(43)	0.54(8)	5.7	–	–
f_{10}	306.0454(18)	3 267.489(19)	1.21(8)	12.7	–	–
f_{11}	331.1260(21)	3 019.998(19)	1.00(8)	10.6	1’	12
f_{12}	363.1588(27)	2 753.616(21)	0.78(8)	8.2	1	11
		Sectors 52,57,59				
f_1	142.6945(45)	7 007.98(22)	0.55(8)	5.6	2	44
f_2	183.4909(35)	5 449.86(10)	0.71(8)	7.2	1’	21
f_3	202.7671(17)	4 931.77(4)	1.45(8)	14.7	1’	19
f_4	214.4968(16)	4 662.075(35)	1.53(8)	15.6	1’	18
f_5	227.8264(44)	4 389.31(8)	0.56(8)	5.7	1’	17
f_6	297.9537(29)	3 356.226(32)	0.86(8)	8.8	2	21
f_7	303.5174(48)	3 294.705(52)	0.51(8)	5.2	1	13
f_8	331.0764(24)	3 020.451(22)	1.03(8)	10.5	1’	12

4. Period fitting

A grid of evolutionary models was calculated using the publicly available and open-source code MESA (Paxton et al. Modules for Experiments in Stellar Astrophysics; 2019, version 11701). A detailed description of the physics and algorithms applied to

https://doi.org/10.1017/pasa.2024.38 Published online by Cambridge University Press

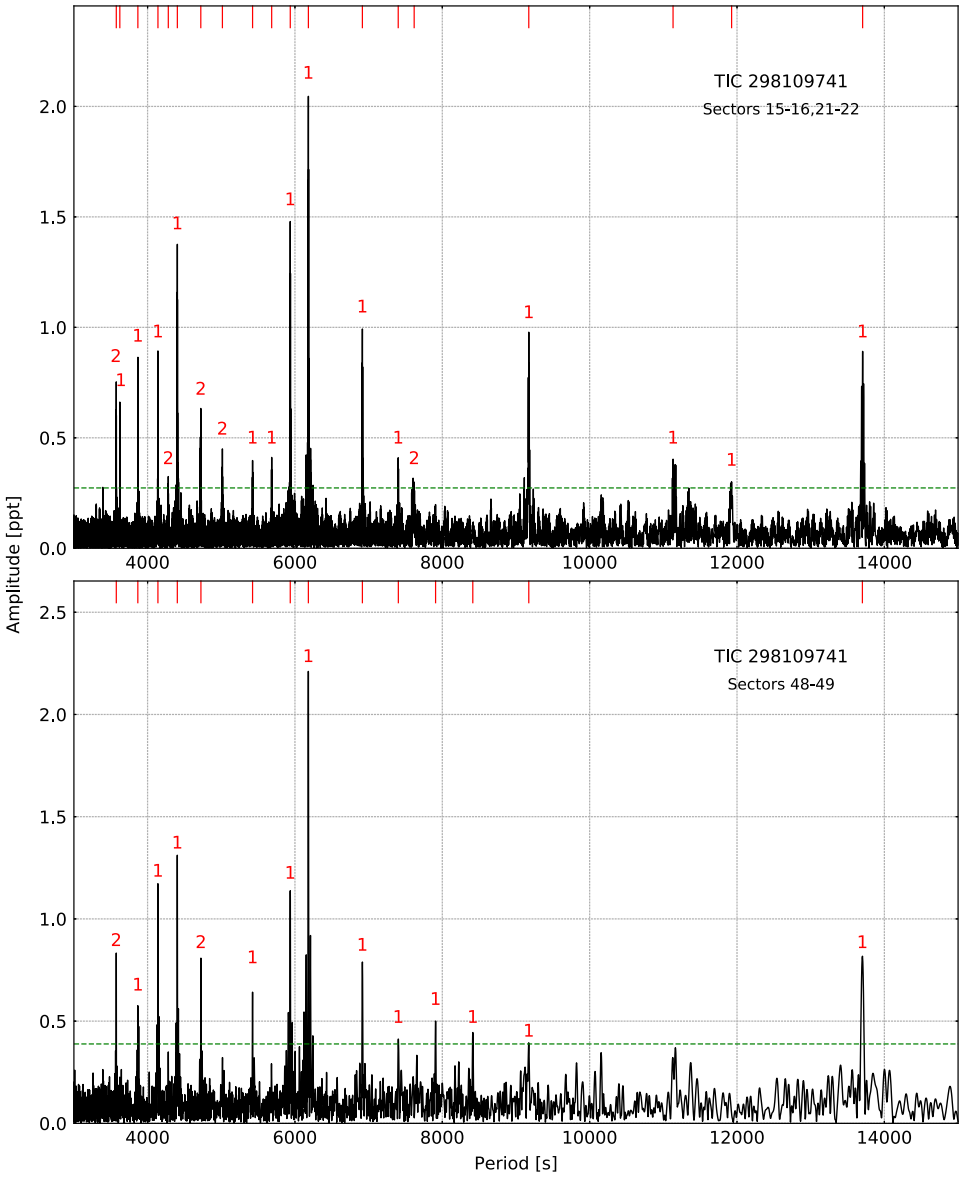

Figure 6. Amplitude spectra calculated from the SC data collected in different TESS sectors for TIC 298109741. The horizontal green dashed line denotes the detection threshold. Modal degrees are shown on top of each identified mode.

calculate the models can be found in Ostrowski et al. (2021) which thoroughly explored MESA models of sdB stars. Newer versions of MESA do not contain any significant improvement in calculating both low to intermediate-mass main sequence and helium-burning EHB stars.

The models were calculated for progenitors with masses in the range 1.0–1.8 $M_\odot$ with 0.005 $M_\odot$ step and metallicities, Z, in the range 0.005–0.035 with 0.005 step. The progenitors evolved to the tip of the red-giant branch where most of the hydrogen has been removed before the helium ignition, leaving only a residual hydrogen envelope on top of the helium core. The envelope masses, M_{env}, are in the range 0.0001–0.0030 $M_\odot$ with 0.0001 $M_\odot$ step, and in the range 0.003–0.010 $M_\odot$ with 0.001 $M_\odot$ step. The models were relaxed to an equilibrium state and evolved until the depletion of helium in the core.

The adiabatic pulsation models were calculated using the GYRE code, version 5.2 (Goldstein and Townsend 2020). The pulsation models were calculated for evolutionary models with central helium abundance, Y_c, in the range 0.9–0.1 with 0.05 increments. The models with $Y_c < 0.1$ were not considered because of the occurrence of the breathing pulses, which are currently an unavoidable side effect of using the convective premixing scheme (Ostrowski et al. 2021).

The calculated grid consists of 63 113 models with pulsation modes calculated up to a modal degree of $l = 4$. We used a goodness-of-fit function, which delivers a difference between observed and calculated periods:

$$S^2 = \frac{1}{N_o} \sum_{i=1}^{N_o} \left(P_o^i - P_c^i\right)^2,$$

https://doi.org/10.1017/pasa.2024.38 Published online by Cambridge University Press

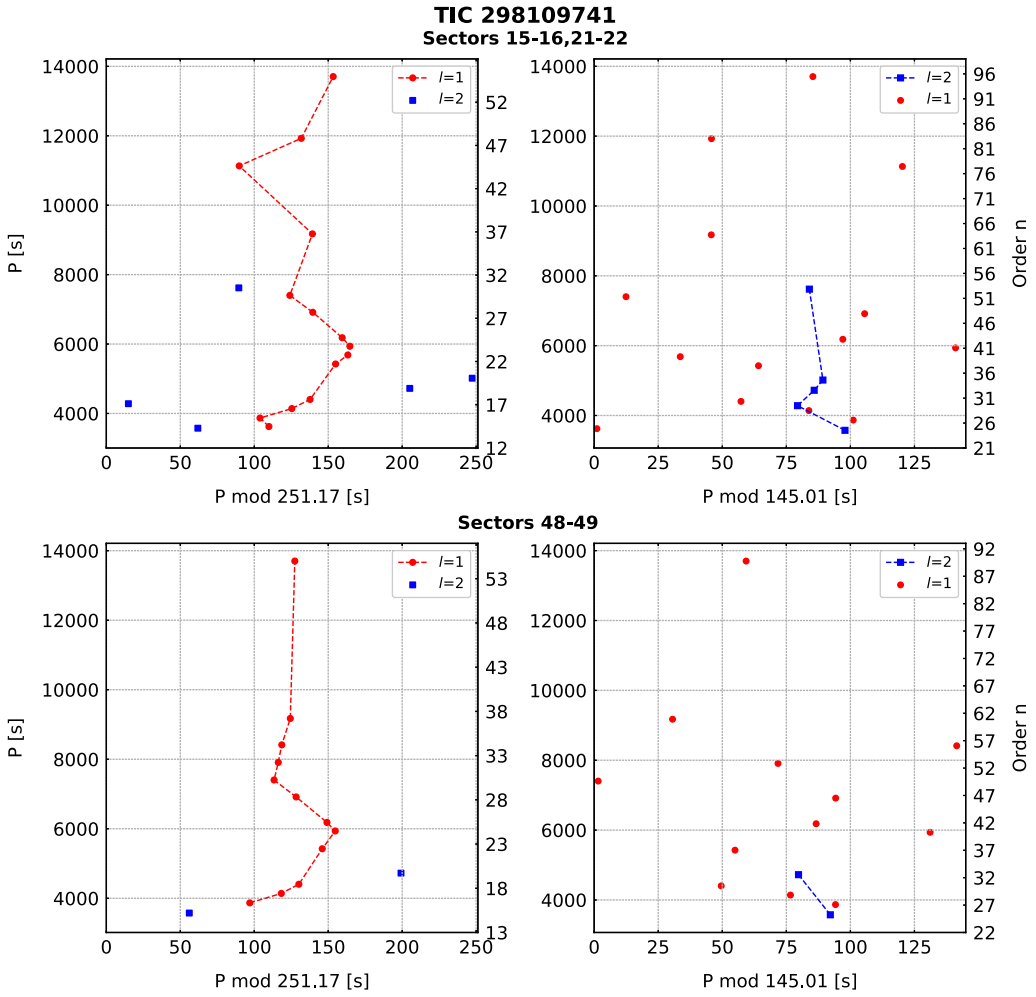

Figure 7. Échelle diagrams for TIC 298109741.

where P_o is an observed period, P_c is a calculated period, and N_o is the number of periods used. The smallest S^2 value indicates the best fit. For our consideration, we accepted all fits up to 1.5 times the minimum value of S^2.

To find the best fit between the models and observations, we adopted the following approach. We applied spectroscopic estimates of T_{eff} and log g (listed in Table 1) and searched the grid of models within three times the uncertainties of both parameters. For TIC 262753627, Table 1 lists two different sets of estimates of spectroscopic parameters, however for the period fitting we adopted only the values derived in this paper. Since our calculated periods are based on adiabatic calculations we used preliminary mode identifications derived in this work. As explained earlier only an asymptotic period spacing was used, which makes the mode identification not necessarily correct. We limited our selection to dipole modes only, and the most convincing periods, that is, high amplitude and/or those detected in both datasets we analysed. For stars with two datasets collected during different Years of the TESS mission, we derived independent solutions for each dataset to check if they are sector-independent. Results of our period fitting are listed in Table 9. There are several caveats, our model tracks cover only core helium fusion, so the core helium fraction will always be > 0, which also places an upper limit on their ages. Also, as explained by Baran and Sanjayan (2023), that is, T_{eff} and log g are subject to large uncertainties, and only adiabatic pulsation periods were considered. Therefore, our period fitting solutions should be taken with caution.

TIC 262753627. We separately fitted periods detected in Sectors 33 and 44–46. All periods used are similar except for the longest period in each dataset. We obtained quite consistent solutions within individual and across the two datasets. The results show that this is a 0.47 $M_\odot$ star, with a radius of either 0.21 or 0.22 $R_\odot$, which came from a progenitor of either 1.7 or 1.75 $M_\odot$. It still has 70% helium in its core, hence it has only been an EHB object for about 30 Myr. The envelope mass is around 0.0027 $M_\odot$, while the mass of the convective core is 0.15 $M_\odot$. For a given progenitor mass there are a few solutions differing in envelope mass. This indicates that period fitting does not constrain the envelope mass particularly well and that small variations in both progenitor mass and envelope mass may deliver comparable sets of calculated pulsation periods.

TIC 269766236. The best solutions constrained by spectroscopic estimates are listed in Table 9. The results show that this is a

https://doi.org/10.1017/pasa.2024.38 Published online by Cambridge University Press

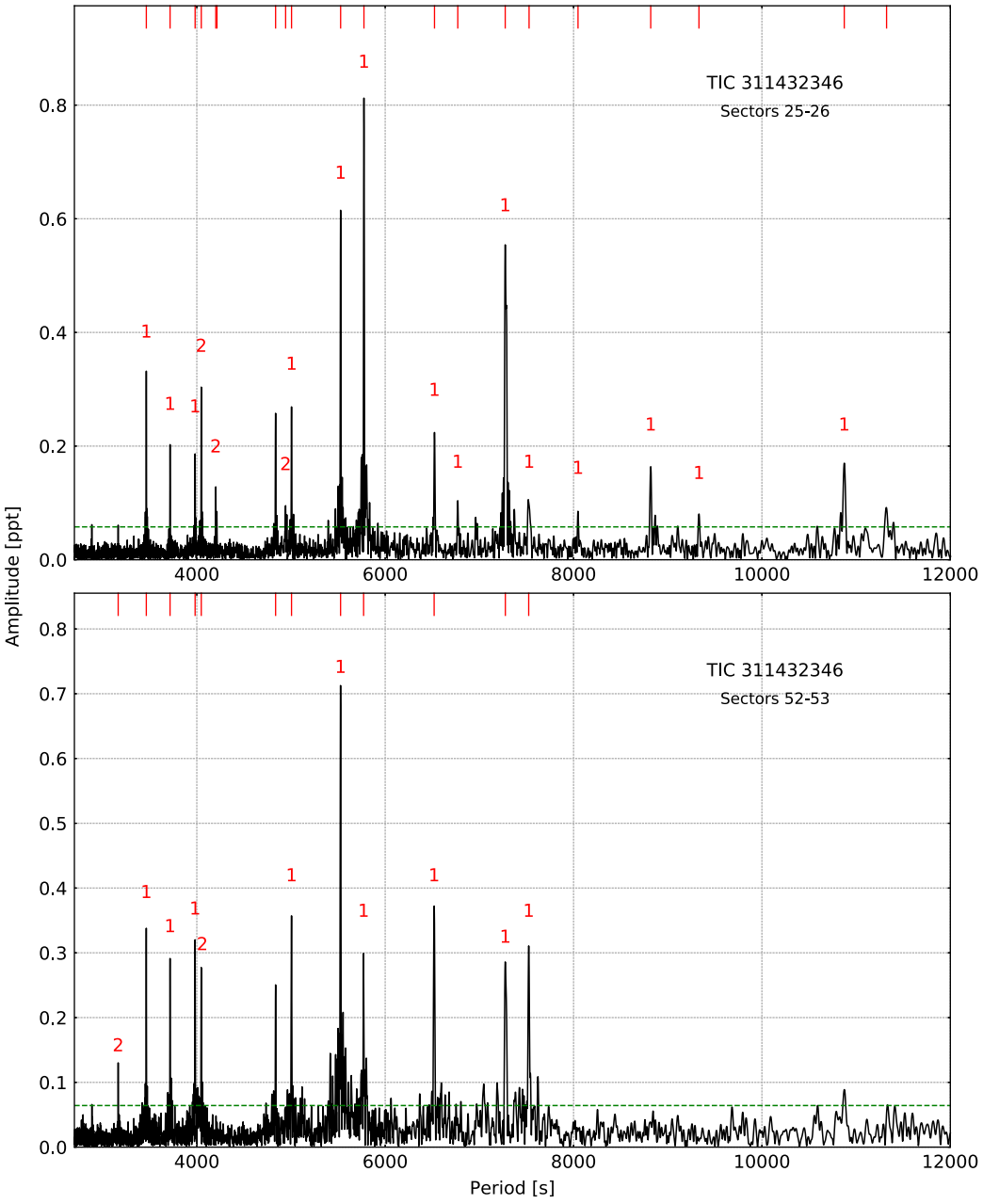

Figure 8. Amplitude spectra calculated from the SC data collected in different TESS sectors for TIC 311432346. The horizontal green dashed line denotes the detection threshold. Modal degrees are shown on top of each identified mode.

0.47 $M_\odot$ star with a radius of either 0.20 or 0.21 $R_\odot$, which came from a progenitor of either 1.60 or 1.65 $M_\odot$. It has 0.45% helium in its core, which corresponds to about 70 Myr age since Zero Age Extreme Horizontal Branch (ZAEHB). The envelope mass is 0.0006 $M_\odot$, on average, while the mass of the convective core is 0.14 $M_\odot$.

TIC 298109741. For both datasets, we derived only one and the same spectroscopically constrained solution, which meets the 1.5 S^2 criterion. The star is a 0.48 $M_\odot$ and 0.20 $R_\odot$ hot subdwarf. It came from a 1.00 $M_\odot$ main sequence star. It still has 0.45 of the central helium to burn, which makes it almost 65 Myr old EHB star. The hydrogen envelope mass is 0.0007 $M_\odot$, while its convective core is 0.15 $M_\odot$.

TIC 311432346. Even though the uncertainty in $T_{\rm eff}$ is quite large we found only three spectroscopic solutions satisfying the 1.5 S^2 criterion in Sectors 25–26 and two solutions in Sectors 52–53. The solutions are very similar and point to a 0.48 $M_\odot$ hot subdwarf with a radius of 0.19 $M_\odot$, which is a descendant of a 1.35–1.50 $M_\odot$ main sequence star. Based on the central helium, it is half way through the EHB stage (60 Myr). It has a hydrogen envelope mass

https://doi.org/10.1017/pasa.2024.38 Published online by Cambridge University Press

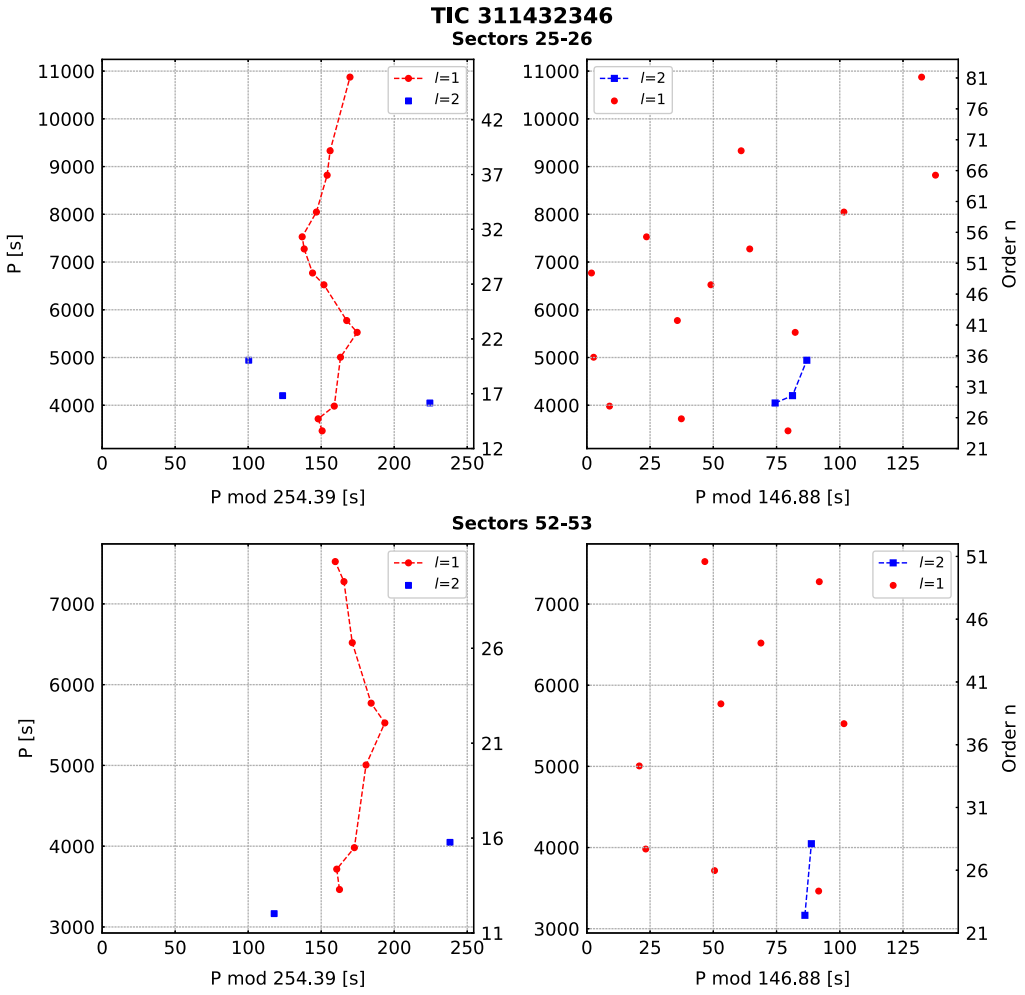

Figure 9. Échelle diagrams for TIC 311432346.

of either 0.0011 or 0.0012 $M_{\odot}$, while the mass of the convective core is 0.15 $M_{\odot}$.

TIC 331553315. This is the only star for which solutions derived from data collected over different cycles, were not closely similar. Instead, the best solutions indicate two possible models with either 0.20 or 0.45 of the central helium. This makes the star either 66 or 110 Myr old EHB object. The mass of the convective core is similar in both solutions – 0.14 or 0.15 $M_{\odot}$. The total mass is 0.47 $M_{\odot}$, while the size ranges between 0.18 and 0.24 $R_{\odot}$. It has evolved from a main sequence progenitor with a mass between 1.70 and 1.80 $M_{\odot}$, while the possible mass of the hydrogen envelope lies between 0.0003 and 0.0026 $M_{\odot}$.

TIC 367003034. We derived only one and the same spectroscopically constrained solution for both datasets. The star is a 0.48 $M_{\odot}$ and 0.20 $R_{\odot}$ hot subdwarf. It evolved from a 1.00 $M_{\odot}$ main sequence star. It still has 0.30 of the central helium to burn, which makes it an almost 85 Myr old EHB star. The hydrogen envelope mass is 0.0006 $M_{\odot}$ while its convective core is 0.15 $M_{\odot}$. This star is very similar to TIC 298109741.

5. Discussion

We aimed to investigate how pulsation modes in hot subdwarfs are related to the helium content and Galactic populations (thin disc, thick disc, halo). We collected a list of 1 587 hot subdwarfs and the relevant information from Luo et al. (2021) and matched the list with the TESS database to retrieve TIC numbers. We found that 40 TIC targets have two different designations in the LAMOST database caused by close stars, and we kept those LAMOST identifiers that were closer to the positions in the Gaia DR3 catalogue (Gaia Collaboration et al. 2023). This resulted in 1 547 targets. We used a list of 330 pulsating hot subdwarfs that we either collected from the literature or found in the TESS data up to Sector 60. We found that 46 pulsators are included in Luo et al. (2021), while $T_{\rm eff}$ and helium content for another 30 pulsators we found in the SIMBAD database. In total, we collected the necessary data for 1 577 hot subdwarfs, including 76 (out of 330) pulsators.

Figure 17 of Luo et al. (2021) shows the helium content in hot subdwarfs. We extend that figure, for the first time, to show the relation between the helium content and the observed pulsations (Fig. 14). The majority of the pulsators are helium-poor hot

https://doi.org/10.1017/pasa.2024.38 Published online by Cambridge University Press

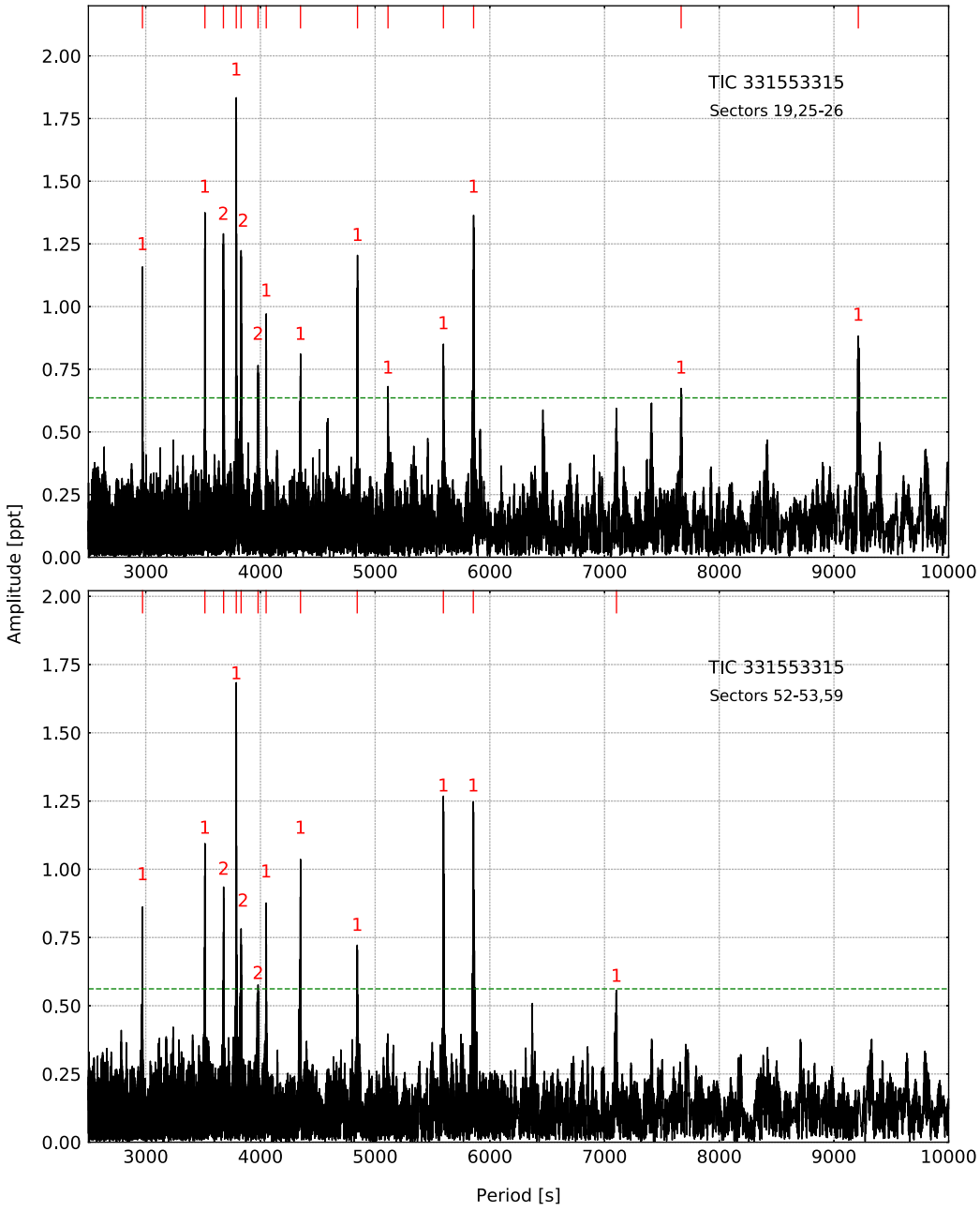

Figure 10. Amplitude spectra calculated from the SC data collected in different TESS sectors for TIC 331553315. The horizontal green dashed line denotes the detection threshold. Modal degrees are shown on top of each identified mode.

subdwarfs including six pulsating subdwarf B stars reported in this paper, while we found no pulsators among the extremely helium-rich hot subdwarfs. We noticed that g-mode pulsators tend to be helium-poor, while p-mode pulsators can be both helium-poor and -weak. According to Figure 1 in Luo et al. (2021), as $T_{\rm eff}$ increases helium becomes more abundant in the atmosphere, so it should be no surprising that g-mode pulsators, which are on the lower $T_{\rm eff}$ end, do not show too much helium in the atmosphere. Three out of four iHe are g-mode pulsators, even though their temperature is well above 30 000 K. These pulsators belong to the group of heavy-metal subdwarfs that show unusual enrichment of elements such as zirconium and lead in their atmospheres. Perhaps this enrichment helps them to pulsate in g-modes even at higher temperatures.

We derived space velocities (U, V, and W), orbital angular momentum (L_z), and orbital eccentricity (e) for 96 pulsators, and modelled Galactic orbits using the `Galpy` python framework (Bovy 2015). The astrometric data (positions, distances, and proper motions) were collected from the Gaia DR3 database. We followed Altmann et al. (2004) and Luo et al. (2021) in determining the Galactic population memberships of our 96 pulsating hot subdwarfs. Memberships of additional 1 547 hot subdwarfs, including 46 pulsators, were taken from Luo et al. (2021).

https://doi.org/10.1017/pasa.2024.38 Published online by Cambridge University Press

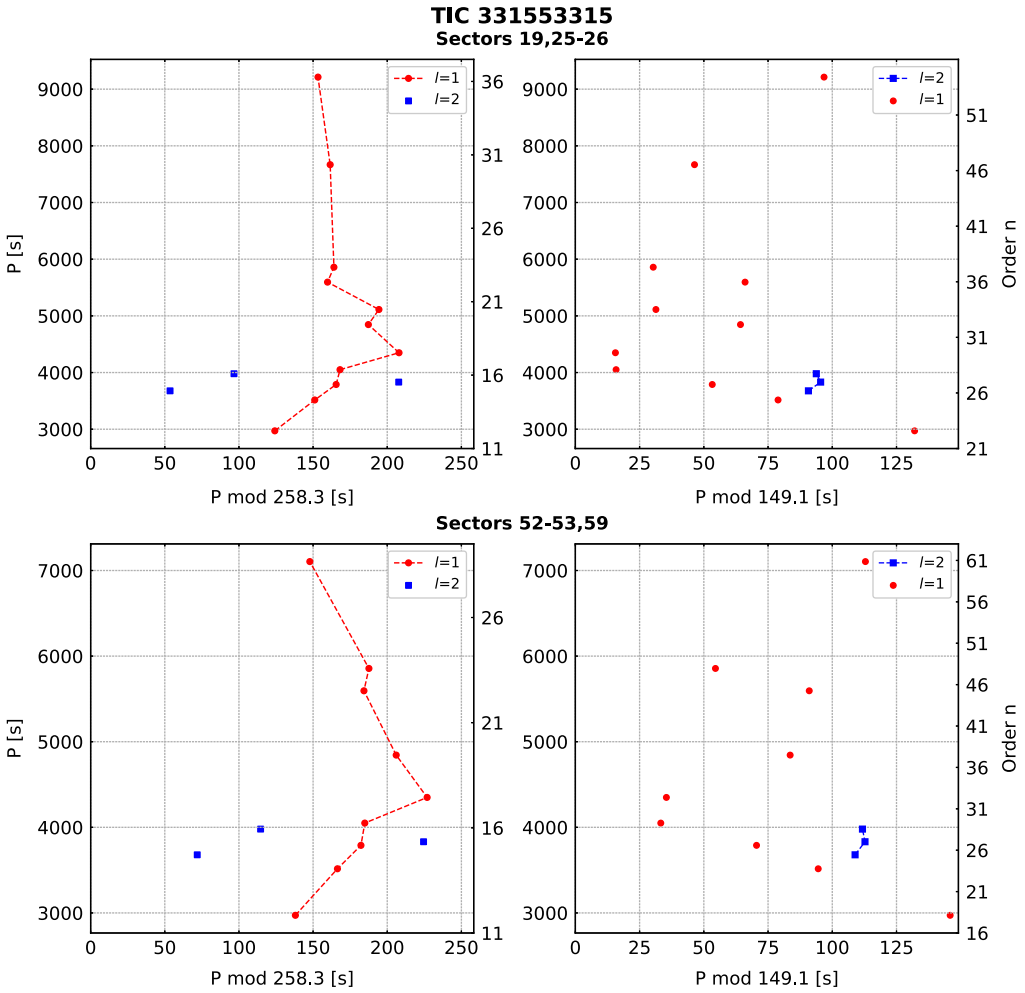

Figure 11. Échelle diagrams for TIC 331553315.

We allocated g-mode, p-mode, and hybrid pulsators to three Galactic populations – thin disc, thick disc, and halo – and show the list of pulsator types in each group in Table 10. The majority of hot subdwarf pulsators belong to the thin and thick disc populations. This is not unexpected, given where the stars are typically born. The halo population is, therefore, more sparse, but it is not yet clear if this is real effect or a bias caused by a limited sample. Our sample is dominated by g-mode pulsators, however we found more p-mode pulsators in the halo population. We stress, however, that we derived Galactic population memberships only for about a third of all pulsating hot subdwarfs in our list and the ratio may change if the size of the sample is increased, and a given Galactic population may show no preference for a specific pulsation type.

6. Summary and discussion

We have presented the results of our analysis of six pulsating hot subdwarfs observed by TESS. We used only the SC data because the USC data provided no additional frequencies in the g-mode region and no p-mode frequencies were detected. Two stars, TIC 262753627 and TIC 367003034, were reported to be pulsators prior to the TESS mission, while TIC 269766236, TIC 298109741, TIC 311432346, and TIC 33155331 were not.

We collected new spectra for four stars, TIC 262753627, TIC 269766236, TIC 298109741, and TIC 367003034, and determined their spectroscopic parameters, that is, $T_{\rm eff}$, log g and log(n(He)/n(H)). For TIC 262753627, TIC 311432346, and TIC 33155331, we cited the atmospheric parameters we found in the literature. We have two independent estimates for TIC 262753627, which turned out to be different within their uncertainties. For further analysis, we accepted the estimates derived from our work.

Except for TIC 269766236, TESS observed stars over multiple sectors. We analysed data collected during two different years (data collected over separate years are denoted as datasets) and used this opportunity to compare the pulsation content. Most of the frequencies we detected exist in two datasets, with a few exceptions. For each star we found between 10 and 20 frequencies that were interpreted as g-mode pulsations. For each dataset, we performed a multiplet search (with a null result) and a mode identification using an asymptotic period spacing. Consequently, we

https://doi.org/10.1017/pasa.2024.38 Published online by Cambridge University Press

Table 9. Models fitting the observed periods of dipole modes within 1.5 S^2, and $T_{\rm eff}$ and log g within three times their uncertainties.

$M_{\rm core}$ ($M_\odot$)	$M_{\rm sdB}$ ($M_\odot$)	$M_{\rm env}$ ($M_\odot$)	M_i ($M_\odot$)	Y_c	$T_{\rm eff}$ (K)	log g	L ($L_\odot$)	R ($R_\odot$)	Age[a] (Myr)
				TIC 262753627 – Sector 33					
0.15	0.47	0.0029	1.75	0.70	24 745	5.43	16.20	0.22	30.15
0.15	0.47	0.0028	1.75	0.70	24 841	5.43	16.20	0.22	30.18
0.15	0.47	0.0030	1.75	0.70	24 651	5.42	16.21	0.22	30.14
0.15	0.47	0.0027	1.75	0.70	24 939	5.44	16.19	0.22	30.21
0.15	0.47	0.0025	1.70	0.70	25 198	5.46	16.38	0.21	29.72
0.15	0.47	0.0026	1.70	0.70	25 094	5.45	16.39	0.21	29.72
0.15	0.47	0.0024	1.70	0.70	25 305	5.47	16.37	0.21	29.76
				TIC 262753627 – Sectors 44–46					
0.15	0.47	0.0030	1.75	0.70	24 651	5.42	16.21	0.22	30.14
0.15	0.47	0.0029	1.75	0.70	24 745	5.43	16.20	0.22	30.15
0.15	0.47	0.0028	1.75	0.70	24 841	5.44	16.20	0.22	30.18
0.15	0.47	0.0026	1.70	0.70	25 094	5.45	16.39	0.21	29.72
0.15	0.47	0.0027	1.70	0.70	24 993	5.44	16.40	0.22	29.71
				TIC 269766236 – Sector 27					
0.14	0.47	0.0006	1.65	0.45	25 888	5.50	16.46	0.20	69.64
0.14	0.47	0.0007	1.65	0.45	25 513	5.47	16.47	0.21	69.58
0.14	0.47	0.0006	1.60	0.45	25 909	5.50	16.53	0.20	69.20
0.14	0.47	0.0005	1.65	0.45	26 254	5.52	16.44	0.20	69.67
				TIC 298109741 – Sectors 15–16,21–22					
0.15	0.48	0.0007	1.00	0.45	27 029	5.52	18.92	0.20	64.45
				TIC 298109741 – Sectors 48–49					
0.15	0.48	0.0007	1.00	0.45	27 029	5.52	18.92	0.20	64.45
				TIC 311432346 – Sectors 25–26					
0.15	0.48	0.0011	1.35	0.50	28 222	5.58	19.71	0.19	57.72
0.15	0.48	0.0011	1.40	0.50	28 004	5.56	19.67	0.19	57.87
0.15	0.48	0.0012	1.50	0.50	27 974	5.56	19.56	0.19	58.25
				TIC 311432346 – Sectors 52–53					
0.15	0.48	0.0012	1.45	0.50	27 996	5.56	19.62	0.19	58.07
0.15	0.48	0.0011	1.35	0.50	28 222	5.58	19.71	0.19	57.72
				TIC 331553315 – Sectors 19,25–26					
0.14	0.47	0.0003	1.75	0.20	28 899	5.61	19.65	0.18	113.55
0.14	0.47	0.0011	1.80	0.20	25 633	5.37	21.34	0.23	110.20
0.14	0.47	0.0012	1.80	0.20	25 409	5.35	21.35	0.24	110.13
0.15	0.47	0.0025	1.70	0.45	25 962	5.43	19.94	0.22	66.26
0.15	0.47	0.0026	1.70	0.45	25 854	5.42	19.95	0.22	66.21
				TIC 331553315 – Sectors 52–53,59					
0.14	0.47	0.0011	1.80	0.20	25 633	5.37	21.34	0.23	110.20
0.15	0.47	0.0025	1.70	0.45	25 962	5.43	19.94	0.22	66.26
0.15	0.47	0.0026	1.70	0.45	25 854	5.42	19.95	0.22	66.21
0.14	0.47	0.0012	1.80	0.20	25 409	5.35	21.35	0.24	110.13
0.15	0.47	0.0026	1.70	0.45	25 545	5.40	19.98	0.23	66.11
				TIC 367003034 – Sectors 17–19,24–25					
0.15	0.48	0.0006	1.00	0.30	28 203	5.52	22.32	0.20	84.80
				TIC 367003034 – Sectors 52,57,59					
0.15	0.48	0.0006	1.00	0.30	28 203	5.52	22.32	0.20	84.80

[a] – age since the Zero Age Extreme Horizontal Branch.

https://doi.org/10.1017/pasa.2024.38 Published online by Cambridge University Press

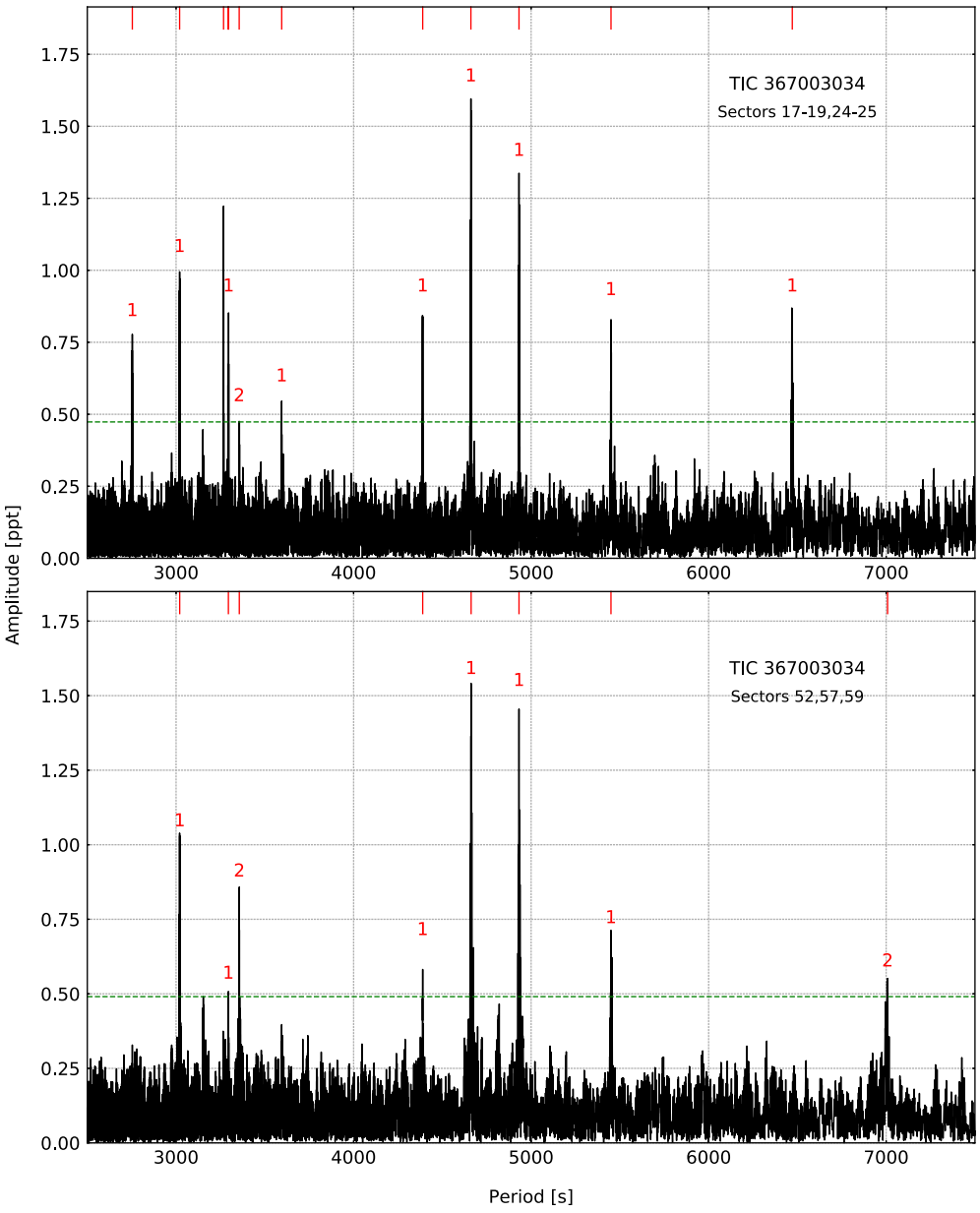

Figure 12. Amplitude spectra calculated from the SC data collected in different TESS sectors for TIC 367003034. The horizontal green dashed line denotes the detection threshold. Mode degrees are shown on top of each identified mode.

derived modal degrees, relative radial orders, and average period spacings for all stars and independently for each dataset. The modal degree assignment does not depend on a dataset, while the average spacing is only different for TIC 367003034. Identification of modes using only the asymptotic period spacing method is not ideal, and hence our mode identifications should be taken with caution. Detection of multiplets in our datasets might have made our mode identifications more robust. Non-detection of any multiplet in the frequency spectrum may be due to a large inclination of the star from the line of sight, a very slow rotation, so the splits of the frequency peaks are smaller than the resolution, or low amplitudes being below the detection threshold we applied.

We used a grid of evolutionary and pulsation models calculated with the `MESA` and `GYRE` to derive the physical parameters of our stars by comparing the observed pulsation periods with the modelled ones. We defined a function S^2 to compare the observed and calculated periods and normalised it by the number of periods used. This function was then used as a criterion to select pulsation models that best fit the observations. We restricted solutions to atmospheric parameters within three times their uncertainties to broaden the grid search and eliminate well-defined but accidental solutions. For each star we obtained either a unique solution or a set of solutions, which differ only slightly in input parameters. The only exception is the central helium content in TIC 331553315.

https://doi.org/10.1017/pasa.2024.38 Published online by Cambridge University Press

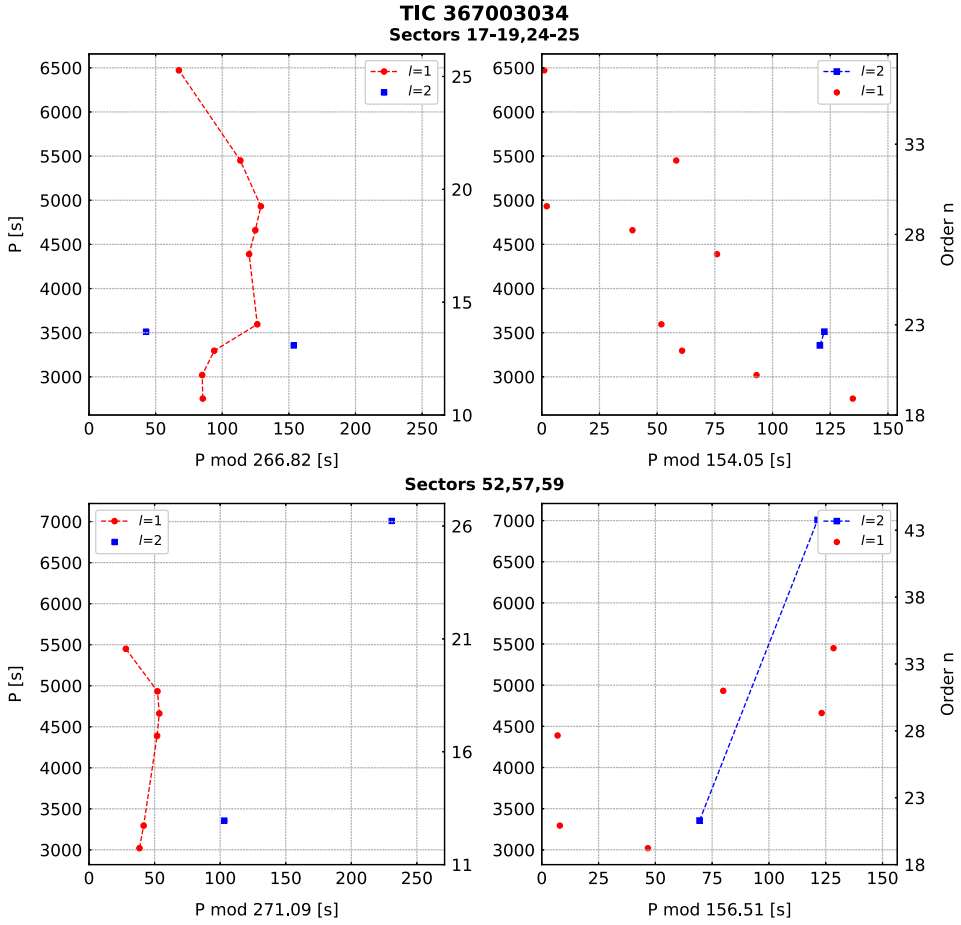

Figure 13. Échelle diagrams derived for TIC 367003034.

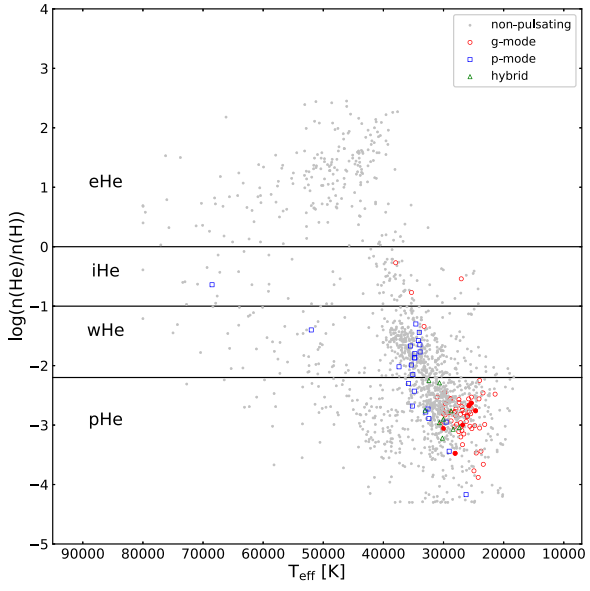

Figure 14. Helium content in function of effective temperature for hot subdwarfs. The four helium group ranges were taken from Luo et al. (2021). The six g-mode rich pulsating subdwarfs that are discussed in this paper are shown with filled circles. Designations we used in the figure follow the ones in Luo et al. (2021), that is, eHe – extreme He-rich, iHe – intermediate He-rich, wHe – He-weak, pHe – He-poor.

We used a sample of 1 577 hot subdwarfs to check the relation between the helium content and pulsations. We found that no pulsators (out of 76) exist among the extremely rich helium hot subdwarfs, while the population of pulsators increases as the helium content decreases. We used a sample of 1 640 hot subdwarfs, including 142 pulsators, to check the distribution of pulsators across the Galactic populations. We found p- and g-mode pulsators in all Galactic populations. Since g-mode pulsators dominate our sample we expected these pulsators to be the most abundant in all populations, however, we found the Galactic halo contains more p-mode pulsators. The number of pulsators in the halo is very small so it may not be a real effect and this trend should be confirmed with a larger sample. This analysis is the first to use a set of pulsating subdwarfs to correlate the pulsation properties with the Galactic populations. A limited sample is the main caveat for such analyses at the moment.

Acknowledgements. Financial support from the National Science Centre Poland under projects No. UMO-2017/26/E/ST9/00703 is acknowledged. P.N. acknowledges support from the Grant Agency of the Czech Republic (GAČR 22-34467S). The Astronomical Institute in Ondřejov is supported by the project RVO:67985815. This paper uses observations made at the South African Astronomical Observatory (SAAO). This research has used the services of www.Astroserver.org. This research made use of `Lightkurve`, a Python package for Kepler and TESS data analysis (Lightkurve Collaboration et al. 2018).

https://doi.org/10.1017/pasa.2024.38 Published online by Cambridge University Press

Table 10. A list of 142 hot subdwarf pulsators allocated to their Galactic populations. The six pulsating subdwarfs presented in this paper are marked in bold and italic.

	g-mode			p-mode			hybrid
Halo		283870336			68495594		
					167746025		
					1204510934		
Thick disc	57257430	178893906		***367003034***	4632676	207440585	
	82049981	194807290		371813244	8787069	219492314	
	122673493	279433960		371833573	47377536	266013993	138618727
	147349694	330658435		381203990	55753808	322009509	355754830
	154510451	332742020		397064286	82359147	437051820	
					115280751	801909110	
Thin disc	4161582	118032308	***269766236***	352480413			
	9346617	118297100	270695353	369394241			
	9358354	120638388	273084007	384992041			
	14680532	121212691	273875093	388940683			
	17561485	138623536	274623605	389175842			
	20448010	138707823	278659026	404635917	6116091	202354658	
	21223262	142491300	281269725	405266556	60985176	240868270	
	26491429	152373379	292467033	405799245	62483415	248949857	13145616
	27782233	156623726	293165262	415339307	63168679	273255412	69298924
	33834484	158215363	***298109741***	418789164	70549283	291032641	169285097
	39947484	158488181	298542142	429807453	136975077	355058528	271164763
	40050637	158918567	309658435	437746793	142200764	366656123	409644971
	43965472	159734503	***311432346***	439905042	165312944	387107334	437043466
	46363456	161402643	317439554	455755305	175402069	396954061	
	63449095	184607974	321287961	457168745	186484490	436579904	
	63719894	219225205	***331553315***	458452988			
	66493797	234295068	334901449	461346891			
	67584818	239930769	344719037	466277784			
	80290366	240109525	345451496	468980287			
	80427831	260795163	347435900	800026675			
	101817287	***262753627***	352315023				

Data availability. The data sets were derived from MAST in the public domain archive.stsci.edu.

References

Altmann, M., Edelmann, H., & de Boer, K. S. 2004, A&A, 414, 181
Baran, A., & Sanjayan, S. 2023, A&A, 73, 21
Baran, A. S., & Koen, C. 2021, A&A, 71, 113
Baran, A. S., Sahoo, S. K., Sanjayan, S., & Ostrowski, J. 2021, MNRAS, 503, 3828
Baran, A. S., et al. 2023, A&A, 669, A48
Baran, A. S., & Winans, A. 2012, A&A, 62, 343
Billères, M., Fontaine, G., Brassard, P., & Liebert, J. 2002, ApJ, 578, 515
Boudreaux, T. M., et al. 2017, ApJ, 845, 171
Charpinet, S., et al. 2019, A&A, 632, A90
Charpinet, S., Fontaine, G., Brassard, P., Chayer, P., Rogers, F. J., Iglesias, C. A., & Dorman, B. 1997, ApJ, 483, L123
Charpinet, S., Giammichele, N., Zong, W., Grootel, V. V., Brassard, P., & Fontaine, G. 2018, OA, 27, 112
Colin, J., et al. 1994, A&A, 287, 38
Crause, L. A., et al. 2019, JATIS, 5, 024007
Dziembowski, W. 1977, A&A, 27, 203
Edelmann, H., Heber, U., Hagen, H.-J., Lemke, M., Dreizler, S., Napiwotzki, R., & Engels, D. 2003, A&A, 400, 939
Fontaine, G., Brassard, P., Charpinet, S., Green, E. M., Randall, S. K., & Van Grootel, V. 2012, A&A, 539, A12
GAIA Collaboration, et al. 2023, A&A, 674, A1
Geier, S., Østensen, R. H., Nemeth, P., Gentile Fusillo, N. P., Gänsicke, B. T., Telting, J. H., Green, E. M., & Schaffenroth, J. 2017, A&A, 600, A50
Geier, S., Raddi, R., Gentile Fusillo, N. P., & Marsh, T. R. 2019, A&A, 621, A38
Goldstein, J. & Townsend, R. H. D. 2020, ApJ, 899, 116
Green, R. F., Schmidt, M., & Liebert, J. 1986, ApJS, 61, 305
Han, Z., Podsiadlowski, P., Maxted, P. F. L., & Marsh, T. R. 2003, MNRAS, 341, 669
Han, Z., Podsiadlowski, P., Maxted, P. F. L., Marsh, T. R., & Ivanova, N. 2002, MNRAS, 336, 449
Heber, U. 2016, PASP, 128, 082001
Hubeny, I. & Lanz, T. 1995, ApJ, 439, 875
Hubeny, I. & Lanz, T. 2017, arXiv e-prints, arXiv:1706.01935
Kaluzny, J. & Rucinński, S. M. 1993, MNRAS, 265, 34
Kilkenny, D., Heber, U., & Drilling, J. S. 1988, South African Astronomical Observatory Circular, 12, 1

https://doi.org/10.1017/pasa.2024.38 Published online by Cambridge University Press

Lei, Z., Zhao, J., Németh, P., & Zhao, G. 2018, ApJ, 868, 70
Lenz, P. & Breger, M. 2005, CoAst, 146, 53
Lightkurve Collaboration, et al. 2018, Astrophysics Source Code Library, record ascl:1812.013
Luo, Y., Németh, P., Wang, K., Wang, X., & Han, Z. 2021, ApJS, 256, 28
Martin, P., Jeffery, C. S., N., N., & Woolf, V. M. 2016, MNRAS, 467, 68
Moehler, S. 2001, PASP, 113, 1162
Moni Bidin, C., Catelan, M., Villanova, S., Piotto, G., Altmann, M., Momany, Y., & Moehler, S. 2008, in Hot Subdwarf Stars and Related Objects, Vol. 392, Astronomical Society of the Pacific Conference Series, ed. U. Heber, C. S. Jeffery, & R. Napiwotzki, 27
Németh, P., Kawka, A., & Vennes, S. 2012, MNRAS, 427, 2180
Østensen, R. H., et al. 2010, A&A, 513, A6
Østensen, R. H., Telting, J. H., Reed, M. D., Baran, A. S., Nemeth, P., & Kiaeerad, F. 2014, A&A, 569, A15
Ostrowski, J., Baran, A. S., Sanjayan, S., & Sahoo, S. K. 2021, MNRAS, 503, 4646
Paxton, B., et al. 2019, ApJSS, 243, 10
Reed, M. D., et al. 2020, MNRAS, 493, 5162
Reed, M. D., Slayton, A., Baran, A. S., Telting, J. H., østensen, R. H., Jeffery, C. S., Uzundag, M., & Sanjayan, S. 2021, MNRAS, 507, 4178
Ricker, G. R., et al. 2014, JATIS, 1, 014003
Sahoo, S. K., et al. 2020a, MNRAS, 495a, 2844
Sahoo, S. K., Baran, A. S., Sanjayan, S., & Ostrowski, J. 2020b, MNRAS, 499b, 5508
Silvotti, R., Németh, P., Telting, J. H., Baran, A. S., østensen, R. H., Ostrowski, J., Sahoo, S. K., & Prins, S. 2022, MNRAS, 511, 2201
Uzundag, M., et al. 2021, A&A, 651, A121
Vos, J., Østensen, R. H., Németh, P., Green, E. M., Heber, U., & Van Winckel, H. 2013, A&A, 559, A54

https://doi.org/10.1017/pasa.2024.38 Published online by Cambridge University Press